ERRATUM PUBLISHED 15 JULY 2026; SEE LAST PAGE
SCIENCE TRANSLATIONAL MEDICINE | RESEARCH ARTICLE

CANCER

Phase separation–based HTS identifies cobimetinib as a YAP-TEAD inhibitor that suppresses hyperactivated YAP-induced cancer progression

Ruizeng Yang[1,2]†, Liqiao Hu[3,4]†, Jing Wang[5]†, Jia Wang[2], Liang Yuan[6], Mengying Wu[3], Lingli He[7], Wentao Yu[7], Peihao Chen[8,9], Xiaoli Lu[10,11], Fangzheng Hu[2], Haijiao Zhang[2], Haoran Gao[7], Xiaodong Wang[1], Haoen Zhang[7], Yang Sun[2], Jinjin Xu[2], Jing Huang[11], Hu Zhou[12,13], Jidong Zhu[14], Fang Wei[2], Yunyun Jin[2,15], Yijun Gao[16], Qiang Fu[1], Xiangbing Qi[8]*, Jing Yu[1,2]*, Pilong Li[5]*, Xiaojing He[17]*, Lei Zhang[1,2,18]*

The Hippo signaling pathway prevents unchecked cell growth, coordinates apoptosis, and preserves proper organ function. Dysregulation of this pathway has been implicated in a myriad of diseases, particularly in cancer. The YAP (Yes-associated protein)–TEAD (TEA domain transcription factor) complex, the key transcriptional downstream effector of the Hippo pathway, hence stands out as an appealing target for therapeutic intervention. In this study, we developed a high-throughput screening (HTS) assay leveraging phase separation principles and found that the US Food and Drug Administration–approved clinical drug cobimetinib is a potent inhibitor of the YAP-TEAD complex. Cocrystallization studies of cobimetinib with TEAD showed that cobimetinib bound to the TEAD lipid pocket and disrupted TEAD palmitoylation. Cobimetinib could overcome resistance to mitogen-activated protein kinase kinase 1/2 inhibitors and to the first-line drug sorafenib in vivo. In addition, cobimetinib suppressed tumor growth and tumorigenesis associated with hyperactivated YAP-TEAD activities in a mouse model of lung cancer. Furthermore, it bolstered the efficacy of the first-line drugs sorafenib and lenvatinib in inhibiting both hepatocellular carcinoma tumor growth and tumorigenesis. These findings establish a strategy for identifying and refining inhibitors of the YAP-TEAD complex in the treatment of cancers driven by aberrant YAP-TEAD activity.

INTRODUCTION

The Hippo signaling pathway is evolutionarily conserved and plays key roles in controlling organ size, maintaining tissue homeostasis, and regulating tumorigenesis. Many of these roles are mediated by the two principal transcriptional effectors, Yes-associated protein (YAP) and transcriptional coactivator with PDZ-binding motif (TAZ), which steer gene expression through binding to the TEA domain transcription factor (TEAD) family of transcription factors. Dysregulated Hippo pathway and YAP/TAZ-TEAD activity are associated with various diseases, especially cancer, making this pathway an attractive therapeutic target (*1*).

YAP/TAZ have surfaced as prominent drivers of human cancers. Their constitutive activation has been demonstrated in liver and mammary gland tumorigenesis (*2*). YAP activation can also sustain tumor growth independently of KRAS in murine models (*3*). In addition, YAP/TAZ contribute to resistance against targeted therapies, such as MEK (mitogen-activated protein kinase kinase) (*4*). Consequently, pharmacological inhibitors targeting the YAP/TAZ-driven transcriptional program hold great potential in cancer therapies, making the YAP/TAZ-TEAD complex a promising drug development target in oncology.

Although there is an apparent absence of druggable pockets in YAP/TAZ, the revelation of a lipid pocket (LP) on TEADs has paved the way for the development and assessment of small-molecule TEAD inhibitors (SMIs) that specifically target TEADs. Various YAP/TAZ-TEAD complex inhibitors have been discovered, mostly allosteric binders that target the TEAD LP, inhibiting autopalmitoylation crucial for TEAD maturation and functionality. However, previous TEAD LP binders exhibited limited efficacy in blocking YAP/TAZ binding to TEADs, resulting in subpar activity and antiproliferative effects. Furthermore, some compounds, like NVP-IAG933, directly compete with YAP/TAZ

[1]Department of Urology, Shanghai Sixth People's Hospital Affiliated to Shanghai Jiao Tong University School of Medicine, Shanghai Eastern Institute of Urologic Reconstruction, Shanghai Jiao Tong University, Shanghai 200233, China. [2]Sheng Yushou Center of Cell Biology and Immunology, School of Life Sciences and Biotechnology, Shanghai Jiao Tong University, Shanghai 200240, China. [3]Key Laboratory of Molecular Biophysics of the Ministry of Education, College of Life Science and Technology, Huazhong University of Science and Technology, Wuhan 430074, China. [4]Guangzhou National Laboratory, Guangzhou 510005, China. [5]State Key Laboratory of Membrane Biology, Frontier Research Center for Biological Structure, School of Life Sciences, Tsinghua University; Tsinghua University-Peking University Joint Center for Life Sciences, Beijing 100084, China. [6]School of Life Science and Technology, ShanghaiTech University, Shanghai 201210, China. [7]Center for Excellence in Molecular Cell Science, Shanghai Institute of Biochemistry and Cell Biology, Chinese Academy of Sciences, University of Chinese Academy of Sciences, Shanghai 200031, China. [8]National Institute of Biological Sciences, 7 Science Park Road, Zhongguancun Life Science Park, Beijing 102206, China. [9]College of Chemistry and Materials Science, Langfang Normal University, Langfang 065000, China. [10]School of Engineering, Xi'an International University, Xi'an 710077, China. [11]School of Life Sciences, Westlake University, Hangzhou 310030, China. [12]Department of Analytical Chemistry, State Key Laboratory of Drug Research, Shanghai Institute of Materia Medica, Chinese Academy of Sciences, Shanghai 201203, China. [13]University of Chinese Academy of Sciences, Beijing 100049, China. [14]Etern Biopharma, Shanghai 201210, China. [15]Shanghai Pudong New Area People's Hospital, Shanghai 201299, China. [16]State Key Laboratory of Oncology in South China, Guangdong Key Laboratory of Nasopharyngeal Carcinoma Diagnosis and Therapy, Sun Yat-sen University Cancer Center, Guangzhou 510060, China. [17]MOE Key Laboratory of Cell Proliferation and Regulation Biology, College of Life Sciences, Beijing Normal University, Beijing 100875, China. [18]School of Life Science, Hangzhou Institute for Advanced Study, University of Chinese Academy of Sciences, Hangzhou 310024, China.
†These authors contributed equally to this work.
*Corresponding author. Email: qixiangbing@nibs.ac.cn (X.Q.); jingyu@sjtu.edu.cn (J.Y.); pilongli@mail.tsinghua.edu.cn (P.L.); hexj@hust.edu.cn (X.H.); rayzhang@sjtu.edu.cn (L.Z.)

at the TEAD binding site. To date, no TEAD binder has received US Food and Drug Administration (FDA) approval (*5*).

The phase separation of YAP is crucial for regulating dynamic changes in genome organization and gene activation, contributing to its oncogenic effects (*6*). In this study, we sought to develop a high-throughput CEBIT (phase-separated condensate-aided enrichment of biomolecular interactions in test tubes)–based assay to identify YAP-TEAD inhibitors, evaluate their ability to curb tumor growth and tumorigenesis (including overcoming drug resistance) across multiple cancer models, and explore their synergistic effects with first-line hepatocellular carcinoma (HCC) drugs.

RESULTS

Cobimetinib is identified as a potential YAP-TEAD binding inhibitor by a CEBIT-based high-throughput screening assay

We established the CEBIT strategy to detect biomolecular interactions previously (*7*). Here, we used this strategy to develop a high-throughput screening (HTS) assay for discovering YAP-TEAD inhibitors. It has been reported that YAP engages with TEADs through three highly conserved interfaces, featuring residues spanning from 50 to 100 (*8*). Thus, by fusing $YAP_{50–100}$ with $(EGFP\text{-}SH3)_{14}$, we generated a construct [$(EGFP\text{-}SH3\text{-}YAP_{50–100})_{14}$] that could be enriched in the phase-separated condensates [$(EGFP\text{-}PRM)_{14}$] and drive phase separation. Similarly, the YAP-binding domain (YBD) of TEAD4 was fused with mCherry to generate mCherry-$TEAD4_{YBD}$. Because of the specific interaction between YAP and TEAD4, mCherry-$TEAD4_{YBD}$ was enriched in the YAP-containing droplets (Fig. 1, A and B). The YAP-TEAD interaction was then quantified by the enrichment of the mCherry signal in enhanced green fluorescent protein (EGFP)–labeled condensates. Mutations at key binding sites of YAP or TEAD4 abolished this enrichment, confirming the system's specificity (fig. S1A). Furthermore, VGLL4, a known TEAD binding competitor of YAP (*9*), also markedly reduced the mCherry signal (fig. S1B). For evaluation of the system's effectiveness in screening YAP-TEAD inhibitors, we tested two known inhibitors: the Super-TDU peptide (*9*) and the VT-104 compound (*10*). With increasing concentrations, both inhibitors progressively decreased mCherry-$TEAD4_{YBD}$ enrichment, as evidenced by reduced mCherry signals (Fig. 1C and fig. S1C). This observation was further substantiated by quantitative analysis of the mCherry/EGFP signal intensity ratio in the droplets (Fig. 1D and fig. S1D). In addition, the HTS assay's *Z*-factor was found to be 0.574 (Fig. 1E), indicative of an excellent assay quality (*11*).

For HTS screening, inhibitors were preincubated with mCherry-$TEAD4_{YBD}$ in 384-well plates for 24 hours. Subsequently, $(EGFP\text{-}SH3\text{-}YAP_{50–100})_{14}$ and $(EGFP\text{-}PRM)_{14}$ were introduced into the system for condensates formation. After an additional 24-hour incubation, high-content imaging was performed on the 384-well plates, and the inhibition effects were assessed by quantifying the mCherry/EGFP signal intensity in the droplets (Fig. 1F). Using this methodology, we screened 6365 diverse compounds, including synthetic chemicals, natural products, and microbial secondary metabolites (fig. S1E), at a concentration of 10 μM. In this screening effort, Super-TDU was used as a reliable positive control to validate the screening process (Fig. 1G). Among the top 10 screened compounds (fig. S1F), cobimetinib emerged as a highly effective inhibitor of the YAP-TEAD interaction (fig. S1, G and H), with an IC_{50} (median inhibitory concentration) value of 7.11 μM (Fig. 1H).

Cobimetinib occupies the palmitoylation site on TEAD and inhibits YAP-TEAD transcriptional activity

We subsequently performed glutathione *S*-transferase (GST) pull-down and microscale thermophoresis (MST) assays. Both assays demonstrated that cobimetinib efficiently disrupted the interaction between YAP and the truncated $TEAD_{YBD}$ in vitro in a dose-dependent manner (Fig. 2, A and B, and fig. S2A). To further investigate whether cobimetinib is capable of disrupting the interaction between YAP and the full-length TEAD in vivo, we performed coimmunoprecipitation experiments with endogenous YAP and TEAD4 in NCI-H226 cells and exogenously expressed YAP and TEAD4 in human embryonic kidney (HEK) 293T cells. The results from both experiments concurred, confirming cobimetinib's ability to interrupt the YAP-TEAD interaction (Fig. 2, C and D, and fig. S2, B and C). The result of CoPIC (compartmentalization of protein-protein interactions in cells), an innovative strategy akin to CEBIT that leverages phase separation for protein-protein interaction screening (*12*), also showed cobimetinib's inhibitory effects on the YAP-TEAD4 interaction (Fig. 2E and fig. S2, D to F).

As a pivotal transcriptional complex, YAP-TEAD binding fosters the expression of vital genes, including *CYR61* and *CTGF*, which govern cell proliferation, migration, and tissue growth. Consequently, we evaluated cobimetinib's impact on these gene expressions. Cobimetinib diminished the expression of YAP-TEAD–regulated genes (Fig. 2F), and impaired YAP-TEAD transcriptional activities, as evidenced by the luciferase reporter assay (Fig. 2G). The repression of YAP-TEAD transcriptional activity could stem from the disruption of their interaction or a defect in YAP's nuclear localization, which is typically controlled by the Hippo kinase cascade–mediated YAP phosphorylation (*13*). Intriguingly, cobimetinib did not alter YAP's nuclear localization (fig. S2G) or the protein abundance of Hippo pathway components, including YAP/TAZ, phosphorylated YAP [pYAP (S127)], and TEAD4 (fig. S2H). Collectively, these findings conclusively established cobimetinib as an effective inhibitor targeting the YAP-TEAD complex and further revealed its primary mode of action: inhibiting YAP function by disrupting the YAP-TEAD interaction.

YAP has been reported to be not therapeutically amenable because of its intrinsically disordered structure (*8*), and numerous reported YAP-TEAD interaction inhibitors tend to function through binding with TEAD (*5*). To determine whether cobimetinib could interact with TEAD, we first generated a biotinylated cobimetinib derivative (biotin-cobimetinib; fig. S2I) and performed biotin pull-down experiments. Biotin-cobimetinib retained similar activity to cobimetinib in suppressing Hippo target *CYR61* expression (fig. S2J), and it was able to pull down TEAD4 in cells, whereas the biotinylated FDA-approved MEK1/2 inhibitor selumetinib (biotin-selumetinib) was not (Fig. 2H and fig. S2K). The binding affinity of cobimetinib for $TEAD4_{YBD}$ was about 1.67 μM as determined by MST analysis (Fig. 2I), and it bound less strongly than VT-104 as determined by surface plasmon resonance analysis (fig. S2L). Moreover, compared with several YAP-TEAD inhibitors (VT-104, K-975, TED-347, MGH-CP1, and GNE 7883), cobimetinib demonstrated stronger inhibition of YAP-TEAD target gene transcription than TED-347 or MGH-CP1 (fig. S3, A and B), and the inhibition was rapid and reached its maximum at 4 hours after treatment (fig. S3B). In addition, similar to VT-104, K-975, and GNE-7883, cobimetinib exhibited greater specificity in suppressing the proliferation of YAP-activated cells, including NCI-H226, NCI-H2052, and NCI-H2373, which are characterized by NF2 inactivation and consequent YAP activation (fig. S4, A and

B). Furthermore, at low concentrations (0.04, 0.12, and 0.37 μM), cobimetinib showed superior inhibitory effects on proliferation in these YAP-activated cell lines compared with MGH-CP1 and TED-347 (fig. S5).

To investigate the molecular dynamics (MD) of cobimetinib in disrupting YAP-TEAD binding, we conducted all-atom MD simulations on five systems containing the TEAD YAP-binding domain: one apo TEAD and four inhibitor-bound systems (with cobimetinib, MGH-CP1, GNE-7883, and VT-105, respectively). Structural analysis revealed that cobimetinib, like the other three compounds, interacted with Cys^{380} of TEAD2 (Cys^{368} of TEAD3), a key residue in the palmitoylation pocket, primarily through hydrogen bonding, alongside hydrophobic interactions with most residues in the binding site (fig. S6A). In addition, the contact number analysis between the

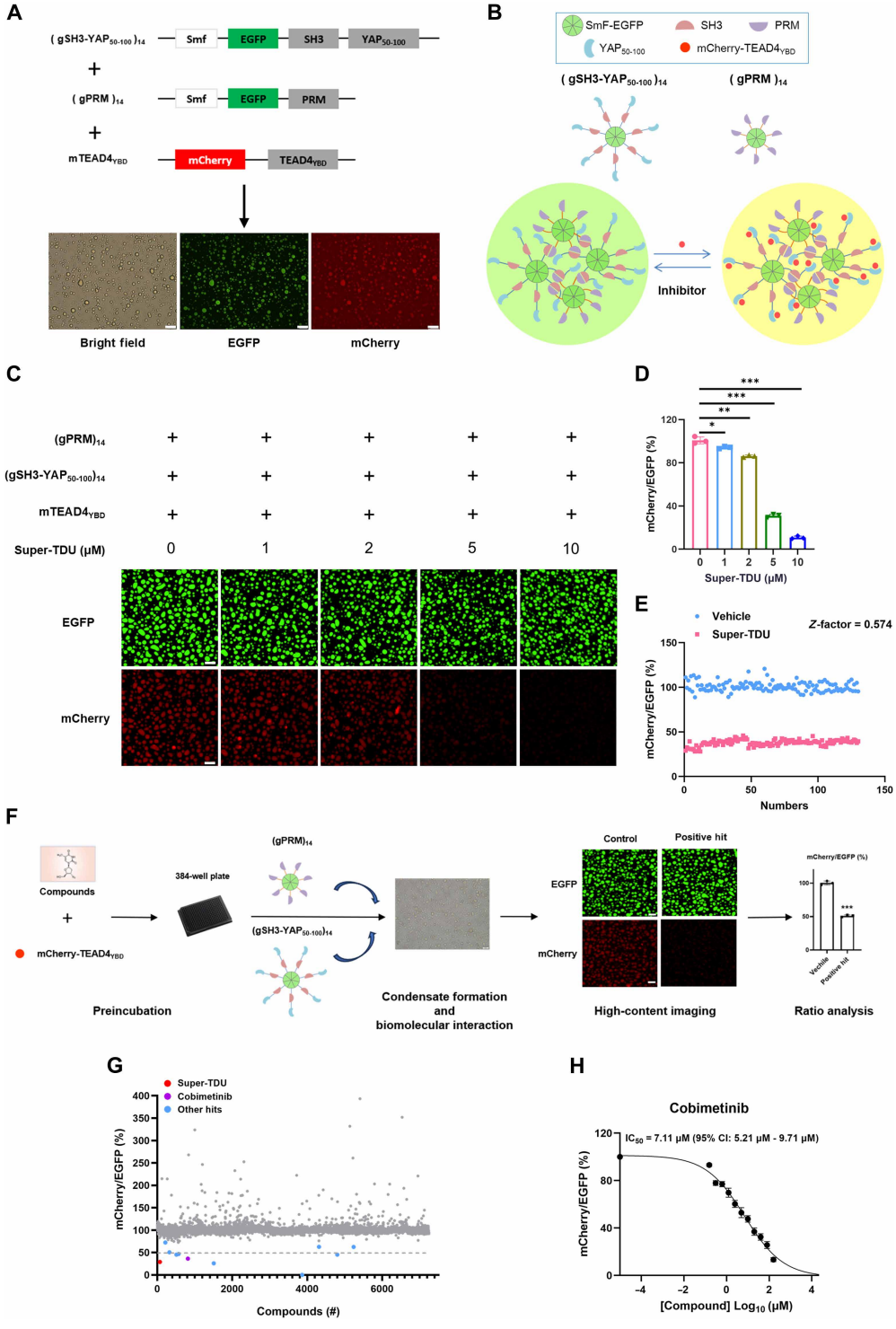

Fig. 1. Cobimetinib is identified as an inhibitor of the YAP-TEAD complex by a CEBIT-based high-throughput screening. (**A**) CEBIT-based assay analyzed $YAP_{50–100}$ and $TEAD4_{YBD}$ interaction. mCherry-$TEAD4_{YBD}$ (0.5 μM) was recruited into phase-separated droplets induced by 0.5 μM each of $(gSH3\text{-}YAP_{50–100})_{14}$ and $(gPRM)_{14}$. Representative fluorescence images depicting the droplets are shown, including views of bright field, EGFP, and mCherry. Scale bars, 10 μm. (**B**) Diagram of the CEBIT-based assay for identifying YAP-TEAD inhibitors. $YAP_{50–100}$ was fused with gSH3 (SmF-EGFP-SH3) to generate $(gSH3\text{-}YAP_{50–100})_{14}$, and $TEAD4_{YBD}$ was fused with mCherry to form mCherry-$TEAD4_{YBD}$. $(gSH3\text{-}YAP_{50–100})_{14}$ and $(gPRM)_{14}$ underwent phase separation, recruiting mCherry-$TEAD4_{YBD}$ into $YAP_{50–100}$-containing droplets. YAP-TEAD inhibitors block mCherry droplet enrichment. (**C**) CEBIT-based assay revealed Super-TDU's dose-dependent inhibition of the YAP-TEAD interaction. Representative EGFP and mCherry images show droplets at different Super-TDU concentrations. Scale bars, 10 μm. (**D**) Quantified mCherry/EGFP fluorescence intensity ratio in droplets at different Super-TDU concentrations ($n = 3$). (**E**) CEBIT-based assay assessed well-to-well reproducibility in 384-well plates. Vehicle and Super-TDU (5 μM) were added as described in (B) ($n = 130$ biological replicates). (**F**) Diagram of CEBIT-based high-throughput screening for identifying YAP-TEAD inhibitors. Candidate compounds were preincubated with mCherry-$TEAD4_{YBD}$, mixed with $(gSH3\text{-}YAP_{50–100})_{14}$ and $(gPRM)_{14}$, and evaluated by droplet mCherry-$TEAD4_{YBD}$ enrichment. (**G**) CEBIT-based assay identified YAP-TEAD inhibitors from 6365 compounds (including synthetic chemicals, natural products, and microbial secondary metabolites) at 10 μM ($n = 1$). Red dot: Super-TDU; purple dot: cobimetinib; blue dots: other hits. (**H**) CEBIT-based assay determined cobimetinib's IC_{50} for inhibiting YAP-TEAD binding ($n = 3$). The curve was fitted by nonlinear regression (4PL model) in GraphPad Prism 10, with the IC_{50} value and its 95% confidence interval (CI) reported. Data are means ± SD. $^*P < 0.05$; $^{**}P < 0.01$; $^{***}P < 0.001$, one-way ANOVA with Tukey's correction. See also fig. S1.

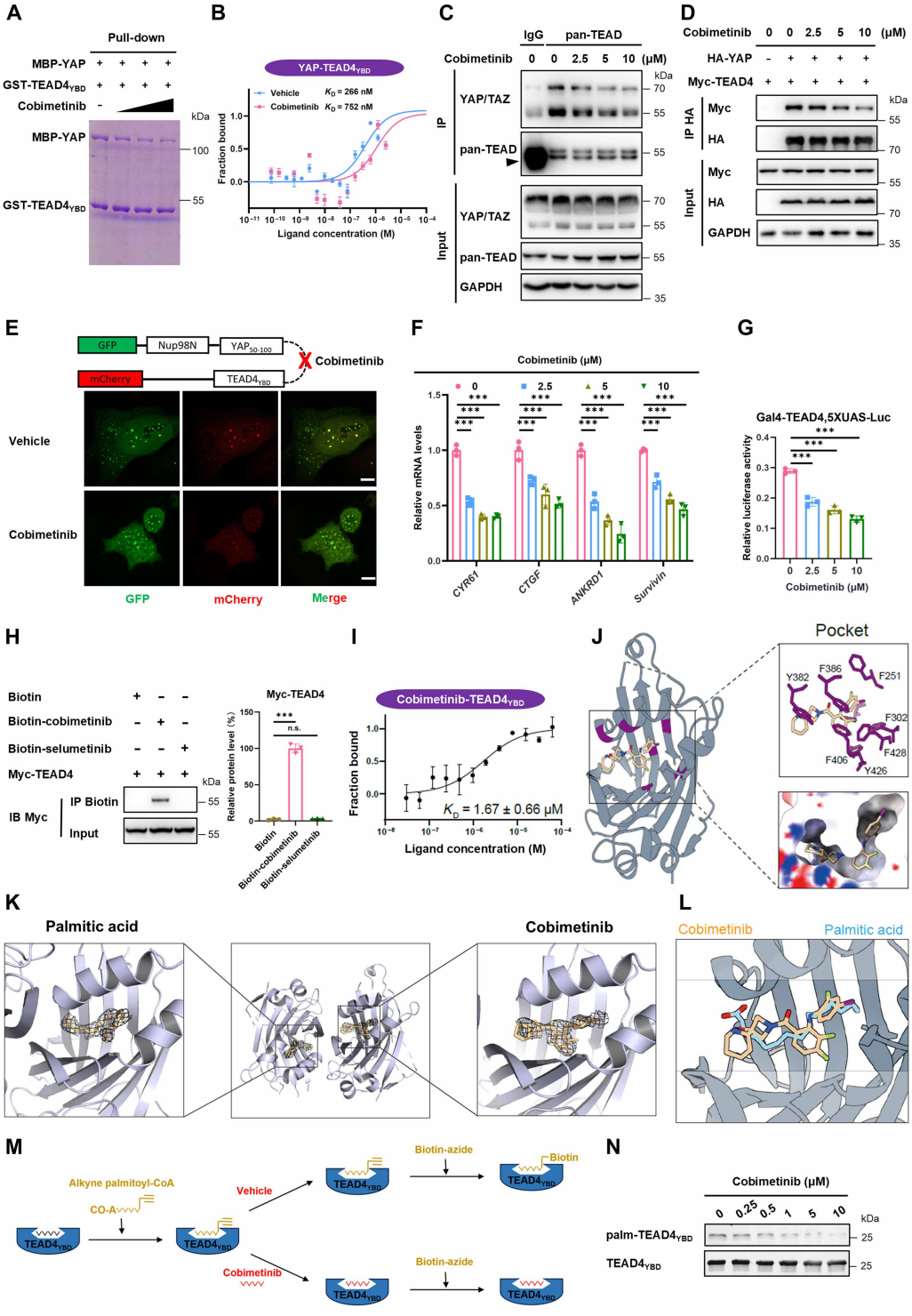

Fig. 2. Cobimetinib disrupts the YAP-TEAD interaction and suppresses the YAP-TEAD transcriptional activities by inhibiting TEAD palmitoylation. (**A**) Pull-down analysis of cobimetinib's dose-dependent disruption of the YAP-TEAD interaction at 0, 10, 20, and 40 μM ($n = 3$). (**B**) MST analysis of the effects of vehicle and cobimetinib (1 mM) on YAP and TEAD4$_{YBD}$ affinity ($n = 3$). (**C**) Coimmunoprecipitation (Co-IP) analysis of vehicle and cobimetinib (2.5, 5, and 10 μM; 12 hours) disrupting endogenous YAP-TEAD4 in NCI-H226 cells ($n = 3$). Arrow, immunoglobulin G (IgG) heavy chain. GAPDH, glyceraldehyde-3-phosphate dehydrogenase. (**D**) Co-IP analysis of vehicle and cobimetinib (2.5, 5, and 10 μM; 12 hours) disrupting exogenous HA-YAP and Myc-TEAD4 interaction in HEK293T cells ($n = 3$). (**E**) CoPIC analysis of cobimetinib (10 μM; 12 hours) inhibiting the YAP-TEAD interaction in HeLa cells coexpressing GFP-Nup98N-YAP$_{50–100}$ and mCherry-TEAD4$_{YBD}$ ($n = 3$). Scale bars, 5 μm. (**F**) RT-qPCR analyzed the dose-dependent effects of cobimetinib (0, 2.5, 5, and 10 μM; 12 hours) on mRNA abundance of YAP-TEAD targets (*CYR61*, *CTGF*, *ANKRD1*, and *Survivin*) in NCI-H226 cells ($n = 3$). (**G**) Gal4-TEAD4 luciferase reporter analysis of cobimetinib's dose-dependent inhibition of YAP transcriptional activities in HEK293T cells. Cells transfected with Gal4-TEAD4, 5XUAS-luciferase, and *Renilla*, treated with cobimetinib at the indicated concentrations for 24 hours, and then luciferase activities were measured and normalized to *Renilla* ($n = 3$). (**H**) Pull-down analysis of the binding of cobimetinib to TEAD4. Cell lysates from HEK293T cells transfected with Myc-TEAD4 were incubated with biotin, biotin-selumetinib, or biotin-cobimetinib before streptavidin pull-down, and immunoblotting was performed to detect TEAD4 binding ($n = 3$). n.s., not significant. (**I**) Microscale thermophoresis analysis of cobimetinib-TEAD4$_{YBD}$ interaction dynamics ($n = 3$). (**J**) Cocrystal structure of TEAD2$_{YBD}$ (gray)–cobimetinib (yellow). TEAD2$_{YBD}$ is shown as carbon, and cobimetinib and surrounding residues (purple) in the deep TEAD2$_{YBD}$ hydrophobic pocket are shown as sticks. (**K**) Simulated annealing $2mF_o - DF_c$ omit map of palmitic acid and cobimetinib bound to TEAD2$_{YBD}$. TEAD2$_{YBD}$ (gray) is shown as carbon, palmitic acid (yellow) and cobimetinib (yellow) are shown as sticks, and the map is shown as black mesh (scaled to 1.0 σ). (**L**) Superposition of cobimetinib (yellow) and palmitic acid [Protein Data Bank (PDB): 5HGU] in the TEAD2$_{YBD}$ (gray) hydrophobic pocket. TEAD2$_{YBD}$ is shown as carbon, and cobimetinib and palmitic acid are shown as sticks. (**M**) Diagram of the in vitro autopalmitoylation assay for TEAD4$_{YBD}$. TEAD4$_{YBD}$ was preincubated with alkyne-modified palmitoyl–coenzyme A (CoA), then vehicle or cobimetinib was added for click chemistry, and palmitoylated TEAD4$_{YBD}$ (palm-TEAD4$_{YBD}$) was detected by streptavidin blot. (**N**) In vitro autopalmitoylation assay analyzed cobimetinib's effects on TEAD4$_{YBD}$ palmitoylation ($n = 3$). Data are means ± SD. ***$P < 0.001$, one-way ANOVA with Tukey's correction. See also figs. S2 to S6.

small molecules and residues lining the binding pocket also demonstrated that cobimetinib, similar to the other three compounds, consistently maintained interactions with the critical palmitoylation residues Cys^{380} and Lys^{357} of TEAD2 (Cys^{368} and Lys^{345} of TEAD3) (fig. S6B). Furthermore, our MD simulations (three replicates per system, each 200 ns in duration) demonstrated a marked reduction in atomic fluctuations of $TEAD_{YBD}$ upon inhibitor binding, suggesting that occupation of the palmitoylation site confers allosteric stabilization of the TEAD surface required for YAP interaction (fig. S6C). To gain a deeper understanding of this intricate interaction, we conducted a cocrystallization experiment of cobimetinib complexed with $TEAD2_{YBD}$, a homolog of $TEAD4_{YBD}$, and resolved its structure at a resolution of 2.7 Å. In this configuration, cobimetinib is deeply embedded in the hydrophobic pocket of TEAD2, surrounded by residues Phe^{251}, Phe^{302}, Tyr^{382}, Phe^{386}, Phe^{406}, Tyr^{426}, and Phe^{428} (Fig. 2J and fig. S6D). Further structural comparison of TEAD2 in complex with cobimetinib or palmitate revealed that cobimetinib occupies the exact same spatial locations as palmitate in the hydrophobic pocket, without inducing any alterations in the folding pattern of TEAD2 (Fig. 2, K and L). Palmitoylation has been reported to be crucial for TEADs binding with YAP and subsequent transcriptional activities (*14*). Consequently, we performed an in vitro autopalmitoylation assay specifically targeting TEAD4 (Fig. 2M). Cobimetinib displayed a dose-dependent inhibitory effect on the palmitoylation of reconstituted $TEAD4_{YBD}$ (Fig. 2N and fig. S6E). These findings suggested that cobimetinib could directly interact with $TEAD4_{YBD}$ and impede the formation of the YAP-TEAD4 complex by inhibiting the palmitoylation of TEAD4.

Cobimetinib overcomes the MEK1/2 inhibitor resistance to inhibit MEK1 mutant tumor growth by targeting the YAP-TEAD complex

Cobimetinib was previously recognized as a highly selective allosteric inhibitor of MEK1/2 (*15*). MEK1/2, an important effector in the RAS signaling cascade, is also implicated in YAP activation (*16*). Given our findings that cobimetinib binds to TEAD and disrupts the interaction between YAP and TEAD, we then investigated the specific effects of cobimetinib's inhibition on the YAP-TEAD interaction, independent of its influence on MEK1/2. To this end, we generated human cervical cancer cells, HeLa with *MEK1/2* double knockout (HeLa-*MEK1/2* DKO). The knockout efficiency was confirmed by genome DNA sequencing (fig. S7A) and immunoblotting (fig. S7B). In addition, we used both selumetinib and PD0325901 (also known as mirdametinib, another selective allosteric MEK1/2 inhibitor) as controls because PD0325901 exhibited inhibitory effects most closely resembling those of cobimetinib, and stronger than those of selumetinib, on the viability of A549 lung cancer cells [harboring the KRAS G12S (Gly^{12}→Ser) point mutation with highly activated MEK1/2 activity], as well as HCT-116 and HT29 colorectal carcinoma cells [both harboring the KRAS G13D (Gly^{13}→Asp) mutation] (fig. S7C). Compared with HeLa wild-type (HeLa-WT) cells, selumetinib, PD0325901, and cobimetinib treatment had no influence on extracellular signal–regulated kinases 1 and 2 (ERK1/2) phosphorylation (Fig. 3A and fig. S7D) or the expression of ERK1/2 downstream genes *FOSL2* and *JUN* (Fig. 3B) in HeLa-*MEK1/2* DKO cells, indicating that selumetinib-, PD0325901-, and cobimetinib-mediated MEK1/2 inhibition was abolished in HeLa-*MEK1/2* DKO cells. However, cobimetinib treatment could still markedly reduce both cell proliferation and colony formation in HeLa-*MEK1/2* DKO cells (Fig. 3, C to E). Furthermore, cobimetinib, but not selumetinib or PD0325901, displayed a marked suppression of *CYR61* and *CTGF* expression in HeLa-*MEK1/2* DKO cells (Fig. 3F). Coimmunoprecipitation experiments indicated that cobimetinib could impair the YAP-TEAD interaction in HEK293T cells, whereas selumetinib and PD0325901 could not (fig. S7E). These data consistently demonstrated that cobimetinib can suppress YAP-TEAD activity by directly targeting the YAP-TEAD interaction, irrespective of MEK1/2 involvement.

MEK1 with an Leu^{98}-Ile^{103} deletion (hereinafter referred to as MEK1 Δ98-103) is a distinctive MEK1 mutant identified in human tumors (*17*), exhibiting hyperactivation of kinase activity (fig. S8A) and robust resistance to allosteric MEK inhibitors (fig. S8B). We found that this MEK1 mutant had the ability to profoundly up-regulate YAP reporter activities (fig. S8C) and to enhance the expression of YAP-TEAD target genes, such as *CYR61* and *CTGF* (fig. S8, A and D). This effect was independent of the Hippo pathway given that *LATS1/2* DKO could not block it (fig. S8, E and F). Moreover, the expression of MEK1 Δ98-103 induced mobility shifts for YAP on SDS–polyacrylamide gel electrophoresis (SDS-PAGE) (fig. S8G) could be reversed by λ phosphoprotein phosphatase (λPP) treatment (fig. S8H), suggesting that MEK1 Δ98-103 triggers a distinct phosphorylation of YAP. ERK1/2, the essential kinases downstream of MEK1/2, have been reported to activate YAP by phosphorylating YAP at multiple sites (*18*). We assumed that ERK1/2 might mediate the promotional effects of MEK1 Δ98-103 on YAP. Consistent with this hypothesis, both the MEK1 Δ98-103–induced upshift (fig. S8I) and enhanced activities of YAP (fig. S8J) were abolished under the condition of ERK1/2 knockdown. Together, these results suggested that MEK1 Δ98-103 could promote YAP phosphorylation through ERK1/2 and augment its transcriptional activity.

Enhanced transcriptional activity of YAP has been reported as a crucial mechanism underlying resistance to MEK1/2 inhibition in RAS-driven neuroblastomas (*19*) and serves as an essential output for tumor progression driven by KRAS mutation (*20*). YAP ablation almost completely abolished MEK1 Δ98-103–induced cell proliferation (fig. S8K) and colony formation (fig. S8, L and M). The ability of MEK1 Δ98-103 to induce YAP-mediated transcription was severely compromised in the TEAD-binding defective YAP–S94A (Ser^{94}→Ala) mutant (fig. S8N), implying the requirement of intact YAP-TEAD transcriptional complexes in mediating the oncogenic MEK1 Δ98-103–induced transcription program. Therefore, cobimetinib was applied as an inhibitor of the YAP-TEAD complex for the treatment of MEK1 Δ98-103–associated tumors in vitro and in vivo. In vitro experiments demonstrated that cobimetinib treatment was more effective in reducing cell proliferation (Fig. 3G) and colony formation (Fig. 3, H and I). Although both PD0325901 and cobimetinib showed comparable inhibitory effects in the A549-WT xenograft mouse model, cobimetinib markedly reduced the tumor growth in the A549-MEK1 Δ98-103 mutant xenograft mouse model, surpassing the efficacy of both PD032590 and selumetinib (Fig. 3, J to M). This superior efficacy correlated with increased apoptosis and decreased proliferation, potentially through inhibition of YAP-TEAD transcriptional activity, without altering phosphorylated ERK1/2 (pERK1/2) or YAP abundance, as assessed by hematoxylin and eosin (H&E) and immunohistochemistry (IHC) staining of Ki67, cleaved caspase-3, pERK1/2, CYR61, and YAP (fig. S9A), and neither cobimetinib nor PD0325901 nor selumetinib affected the body weight of the mice (fig. S9B). Furthermore, cobimetinib markedly suppressed the expression of YAP-target genes *CYR61* and *CTGF* compared with selumetinib

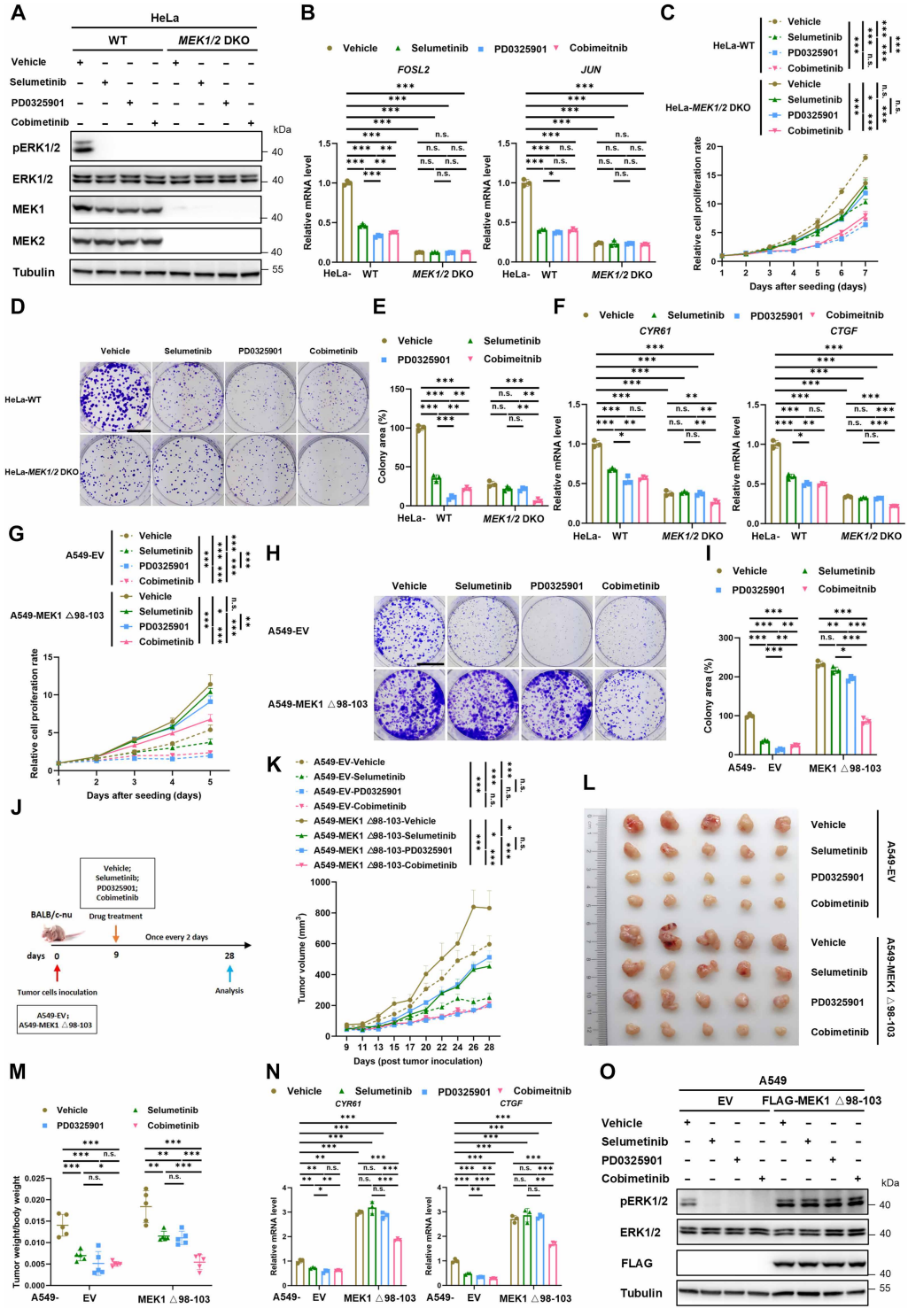

Fig. 3. Cobimetinib reduces human MEK1 mutant tumor growth by targeting the YAP-TEAD complex. (**A**) Immunoblotting analyzed vehicle, selumetinib (5 μM), PD0325901 (5 μM), and cobimetinib (5 μM) effects on ERK1/2 activation in HeLa WT and *MEK1/2* DKO cells ($n = 3$). (**B**) RT-qPCR analyzed vehicle, selumetinib (5 μM), PD0325901 (5 μM), and cobimetinib (5 μM) effects on the expression of ERK1/2 downstream genes *FOSL2* and *JUN* in HeLa-WT and *MEK1/2* DKO cells. (**C**) Cell proliferation assay analyzed the effects of vehicle, selumetinib (5 μM), PD0325901 (5 μM), and cobimetinib (5 μM) on cell proliferation in HeLa-WT and *MEK1/2* DKO cells. (**D**) Colony formation assay analyzed the effects of vehicle, selumetinib (5 μM), PD0325901 (5 μM), and cobimetinib (5 μM) on colony formation in HeLa-WT and *MEK1/2* DKO cells ($n = 3$). Scale bar, 1 cm. (**E**) Quantified relative colony area described in (D). (**F**) RT-qPCR analyzed the effects of vehicle, selumetinib (5 μM), PD0325901 (5 μM), and cobimetinib (5 μM) on the expression of YAP-TEAD downstream genes *CYR61* and *CTGF* in HeLa-WT and *MEK1/2* DKO cells. (**G**) Cell proliferation assay analyzed the effects of vehicle, selumetinib (1 μM), PD0325901 (1 μM), and cobimetinib (1 μM) on cell proliferation in A549 wild-type (WT) and MEK1 Δ98-103 mutant cells. (**H**) Colony formation assay analyzed the effects of vehicle, selumetinib (1 μM), PD0325901 (1 μM), and cobimetinib (1 μM) on colony formation in A549-WT and MEK1 Δ98-103 mutant cells ($n = 3$). Scale bar, 1 cm. (**I**) Quantified relative colony area described in (H). (**J**) Treatment diagram for vehicle, selumetinib, PD0325901, and cobimetinib in the A549-WT and MEK1 Δ98-103 mutant CDX tumor growth model. (**K**) Tumor growth curve of vehicle, selumetinib (5 mg/kg), PD0325901 (5 mg/kg), and cobimetinib (5 mg/kg) treatment in the A549-WT and MEK1 Δ98-103 mutant CDX mice model ($n = 5$). (**L**) Representative tumor images described in (J) and (K) were documented on day 28 post-inoculation. (**M**) The ratio of tumor weight to body weight described in (J) to (L) was calculated on day 25 postinoculation ($n = 5$). (**N**) RT-qPCR assessed the effects of vehicle, selumetinib (5 μM), PD0325901 (5 μM), and cobimetinib (5 μM) on the mRNA abundance of the YAP-TEAD target genes *CYR61* and *CTGF* in A549-WT and MEK1 Δ98-103 mutant cells ($n = 3$). (**O**) Immunoblotting analyzed the effects of vehicle, selumetinib (5 μM), PD0325901 (5 μM), and cobimetinib (5 μM) on ERK1/2 phosphorylation in A549-WT and MEK1 Δ98-103 mutant cells ($n = 3$). Data are means ± SD. *$P < 0.05$; **$P < 0.01$; ***$P < 0.001$; n.s., not significant; one-way ANOVA with Tukey's correction. See also figs. S7 to S10.

and PD0325901 in A549-MEK1 Δ98-103 cells (Fig. 3N) while maintaining the abundance of pERK1/2 (Fig. 3O and fig. S9C). Cobimetinib induced dose-dependent inhibition of MAPK targets (*FOSL2* and *JUN*) and Hippo targets (*CYR61* and *CTGF*). However, only MAPK target inhibition was reversed by constitutively active MEK1 overexpression (Fig. 2F and fig. S9, D and E), demonstrating that cobimetinib suppresses YAP activity and tumor growth through direct disruption of the YAP-TEAD interaction.

In addition, another cell line resistant to the MEK1/2 inhibitor trametinib (A549-TramR) was generated and validated using cell viability and colony formation assays (fig. S10, A to C). Activation of both YAP and MAPK signaling in A549-TramR cells was evidenced by decreased phosphorylation of YAP [pYAP (S127)] and increased pERK1/2 (fig. S10D). This resistant cell model was then used to assess cobimetinib's efficacy in overcoming MEK1/2 inhibitor resistance mediated by the YAP-TEAD complex. Cobimetinib, unlike selumetinib or PD0325901, reduced colony formation in A549-TramR cells (fig. S10, E and F). Together, these findings provided further evidence that cobimetinib inhibited YAP activity and tumor growth by directly targeting the YAP-TEAD interaction. They also suggested that cobimetinib might be a promising therapeutic option for cancers with the MEK1 Δ98-103 mutant and those that are resistant to conventional MEK1/2 inhibitors.

Cobimetinib suppresses YAP-hyperactivated tumor growth through targeting the YAP-TEAD complex

Aberrant hyperactivation of YAP/TAZ has been implicated in contributing to oncogenesis, fostering cancer cell proliferation, enhancing metastasis, and inducing therapy resistance (*2*). In this study, we further explored the efficacies of cobimetinib on inhibiting cell viability and tumor growth of YAP-hyperactivated cancer cells. Neurofibromatosis type 2 (NF2) deficiency, a biomarker for YAP dependency, is prevalent in mesothelioma and triggers YAP/TAZ activation (*21*). Large tumor suppressor kinases 1 and 2 (LATS1/2), the core kinases of the Hippo signaling pathway, mediate the phosphorylation of YAP and suppress its oncogenic function (*13*); thus, the *LATS1/2* double knockout cells (*LATS1/2* DKO) exhibit the hyperactivation of YAP-TEAD function. Undoubtedly, compared with PD0325901, cobimetinib showed superior inhibitory effects on cell viability across a range of NF2-null mesothelioma cell lines, including NCI-H226 (Fig. 4A), NCI-H2052 (fig. S11A), NCI-H2373 (fig. S11A), and NCI-H2373 (fig. S11B), as well as HeLa-*LATS1/2* DKO cells (Fig. 4B).

Furthermore, compared with selumetinib and PD0325901, cobimetinib markedly impeded tumor growth of NCI-H226 cells, recapitulating its mechanism observed in the A549-MEK1 Δ98-103 model through increased apoptosis and reduced proliferation through inhibition of YAP-TEAD transcriptional activity (Fig. 4, C to F, and fig. S11C) without affecting mice's body weight (fig. S11D). Moreover, although PD0325901 and cobimetinib exhibited similar inhibition effects in the HeLa CDX mouse model (fig. S12, A to F), cobimetinib was much more potent at inhibiting the HeLa-*LATS1/2* DKO tumor growth than PD0325901 in vivo through mechanisms similar to those observed in the A549-MEK1 Δ98-103 mutant model (Fig. 4, G to J, and fig. S13, A and B). In addition, reverse transcription quantitative polymerase chain reaction (RT-qPCR) analysis of Hippo target gene expression in these xenograft tumors revealed that cobimetinib surpassed PD0325901 in decreasing the mRNA abundance of Hippo target genes, including *CYR61*, *CTGF*, and *ANKRD1* (Fig. 4, K and L). Besides, *LATS1/2* DKO in HeLa cells further enhanced cobimetinib sensitivity (Fig. 4M), whereas *TEAD1/3/4* (Fig. 4N) and *YAP/TAZ* (Fig. 4O) knockdown in HeLa cells, as well as TEAD knockout in YAP-5SA–overexpressing HEK293A cells (fig. S14, A and B), reduced it, reinforcing our findings that cobimetinib targeted the YAP-TEAD complex. Moreover, we also generated a constitutively active TEAD mutant cell line in NCI-H2373 cells by overexpressing TEAD4-VP16 (designated as NCI-H2373-TEAD4-VP16) for rescue experiments. The cell line was validated by assessing the expression of TEAD4-VP16-FLAG and YAP-TEAD target genes (fig. S14, C and D). Compared with NCI-H2373-WT cells, the inhibitory effects of cobimetinib on YAP-TEAD target genes were completely abolished in NCI-H2373-TEAD4-VP16 cells (fig. S14E). In addition, the suppressive effects of cobimetinib on cell colony formation were also markedly attenuated in NCI-H2373-TEAD4-VP16 cells (fig. S14, F and G). These findings further confirmed that cobimetinib targeted the YAP-TEAD complex.

In line with a sensitivity analysis of 81 liver cancer cells, collecting 31 public liver cancer cell lines and 51 patient-derived cell models, to 90 anticancer drugs, including three MEK1/2 inhibitors—cobimetinib, trametinib, and selumetinib (*22*)—liver cancer cells with high *TEAD1* expression were more sensitive to cobimetinib than trametinib or selumetinib (Fig. 4, P to Q, and fig. S14, H to I). Collectively, these results underscored cobimetinib's ability to inhibit YAP-TEAD activities and demonstrate its enhanced efficacy against tumors with YAP addiction.

Cobimetinib inhibits both liver tumor growth and tumorigenesis and alleviates liver damage

The activation of YAP has been revealed to promote liver cancer development and liver tumorigenesis (*23*–*25*). YAP has also been reported to be overexpressed in various patient-derived HCC tissues (*26*). The Huh7 hepatoma cell line is Hippo inactive (*27*) and exhibits high YAP expression (*28*). Compared with HepG2, Mahlavu, and Hep3B HCC cells, a high protein abundance of YAP/TAZ and TEADs was observed in Huh7 cells (fig. S15A). YAP knockdown reduced both cell proliferation and colony formation in Huh7 cells as well (fig. S15, B to E). Therefore, we selected the Huh7 model to further evaluate the efficacy of cobimetinib. Beyond its marked effectiveness in suppressing the growth of MEK mutant (Fig. 3) and YAP-hyperactivated tumors (Fig. 4), cobimetinib undeniably demonstrated superior inhibitory effects on Huh7 liver cancer tumor growth compared with selumetinib and PD0325901, both in vitro and in vivo (Fig. 5, A to G, and fig. S15, F to J). The underlying mechanisms were similar to those in the aforementioned cobimetinib-treatment models (fig. S15K). In addition, cobimetinib showed better suppression of the metastasis of Huh7 liver cancer cells in vitro (fig. S15, L to O).

Moreover, we explored the impact of cobimetinib on liver tumorigenesis in three mouse models. Extensive research has shown that YAP, acting downstream of proto-oncoprotein Myc or aberrant p53, contributes to carcinogenesis. Therefore, we first used a well-established genetic mouse model that mimics human HCC driven by *Myc* overexpression and *p53* knockout (Myc; sg-*p53*) (Fig. 5H). This model generates liver tumors in a relatively short period of 3 to 4 weeks, recapitulating all the histologic features of human HCC (*29*). After 3 weeks of treatment with PD0325901 and cobimetinib, the mice's livers were dissected for further analysis. Cobimetinib treatment drastically repressed liver tumorigenesis (Fig. 5, I and J). The reduction in serum ALT (alanine aminotransferase) and AST (aspartate aminotransferase) concentrations after cobimetinib treatment indicated that improved liver function resulted from alleviating tumorigenesis (Fig. 5, K and L), and the minimal changed body weights also implied low toxicity of the drug (fig. S16A). Furthermore, pathological analysis revealed that the cobimetinib-treated group had much smaller lesions, a lower proliferation rate, and a higher apoptosis rate compared with those of the vehicle- or PD0325901-treated group (Fig. 5, M and N, and fig. S16B). In addition, cobimetinib treatment inhibited the expression of Hippo targets (Fig. 5O and

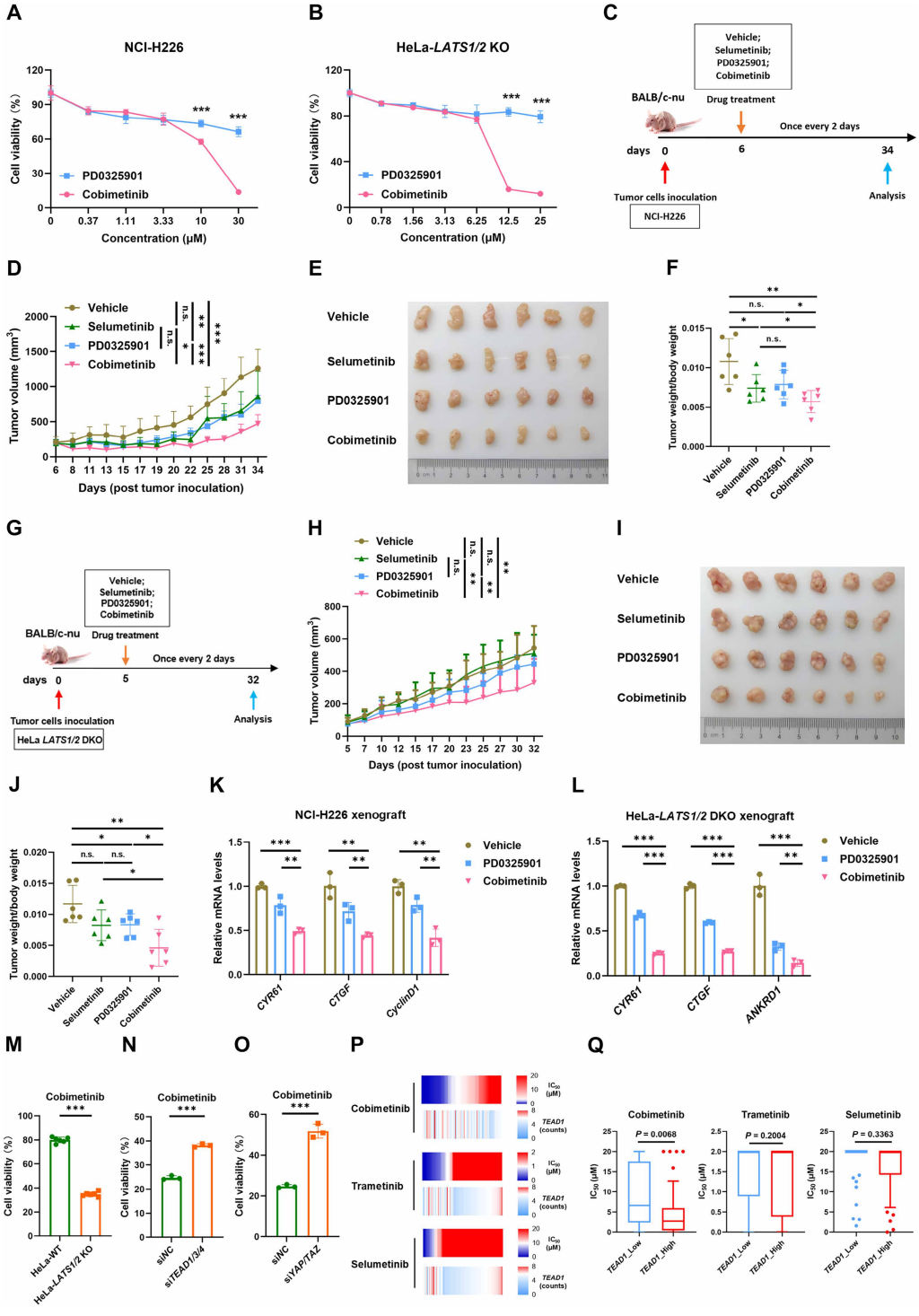

Fig. 4. Cobimetinib inhibits YAP-hyperactivated tumors growth by directly targeting the YAP-TEAD complex. (**A** and **B**) Cell viability assay assessed the effects of PD0325901 and cobimetinib on cell viability in NCI-H226 [(A); $n = 6$] and HeLa-*LATS1/2* DKO cells [(B); $n = 6$]. (**C**) Treatment diagram for vehicle, selumetinib, PD0325901, and cobimetinib in the NCI-H226 CDX tumor growth model. (**D**) Tumor growth curve of vehicle, selumetinib (10 mg/kg), PD0325901 (10 mg/kg), and cobimetinib (10 mg/kg) treatment in the NCI-H226 CDX ($n = 6$) tumor growth model. (**E**) Representative tumor images described in Fig. 3 (C and D) were documented on day 34 postinoculation. (**F**) The ratio of tumor weight to body weight described in Fig. 3 (C to E) was calculated on day 34 postinoculation ($n = 6$). (**G**) Treatment diagram for vehicle, selumetinib, PD0325901, and cobimetinib in the HeLa-*LATS1/2* DKO CDX tumor growth model. (**H**) The tumor growth curve of vehicle, selumetinib (10 mg/kg), PD0325901 (10 mg/kg), and cobimetinib (10 mg/kg) treatment in the HeLa-*LATS1/2* DKO CDX tumor growth model ($n = 6$). (**I**) Representative tumor images described in Fig. 3 (G and H) were documented on day 32 postinoculation. (**J**) The ratio of tumor weight to body weight described in Fig. 3 (G to I) was calculated on day 32 postinoculation ($n = 6$). (**K**) RT-qPCR analyzed the expression of YAP-TEAD target genes *CYR61*, *CTGF*, and *CyclinD1* in NCI-H226 xenograft described in Fig. 3 (C to F) ($n = 3$). (**L**) RT-qPCR analyzed the expression of YAP-TEAD target genes *CYR61*, *CTGF*, and *ANKRD1* in HeLa-*LATS1/2* DKO xenograft described in Fig. 3 (G to J) ($n = 3$). (**M** to **O**) Cell viability analysis assessed *LAST1/2* DKO [(M); $n = 6$], *TEAD1/3/4* knockdown (si*TEAD1/3/4*) [(N); $n = 3$], and *YAP/TAZ* knockdown (si*YAP/TAZ*) [(O); $n = 3$] effects on HeLa cell sensitivity to cobimetinib. (**P**) Correlation analysis of cell sensitivity (IC_{50}) ($n = 3$) of MEK1/2 inhibitors cobimetinib, trametinib, and selumetinib with *TEAD1* expression ($n = 2$) in 81 liver cancer cell lines by GraphPad Prism 10. IC_{50} values of cobimetinib, trametinib, and selumetinib as well as *TEAD1* expression of 81 liver cancers were downloaded from the LIMORE database. The top panel shows the IC_{50} (blue: sensitivity; red: resistance), and the bottom panel shows the TEAD1 expression (blue: low; red: high). (**Q**) Quantified correlation of the IC_{50} of cobimetinib, trametinib, and selumetinib with *TEAD1* expression in 81 liver cancer cell lines as described in Fig. 3P by GraphPad Prism 10. *TEAD1*_Low and *TEAD1*_High represented the bottom and top 30% of the *TEAD1* expression. For a box-and-whisker plot, the box displays the IC_{50} IQR (interquartile range), with the internal line indicating the median. Whiskers extend to Q3 + 1.5 × IQR and Q1 − 1.5 × IQR, and points beyond are outliers. Data are means ± SD. $^*P < 0.05$; $^{**}P < 0.01$; $^{***}P < 0.001$; n.s., not significant; Student's *t* test [(A), (B), and (M) to (O)]; one-way ANOVA with Tukey's correction [(D), (F), (H), and (J) to (L)]. See also figs. S11 to S14.

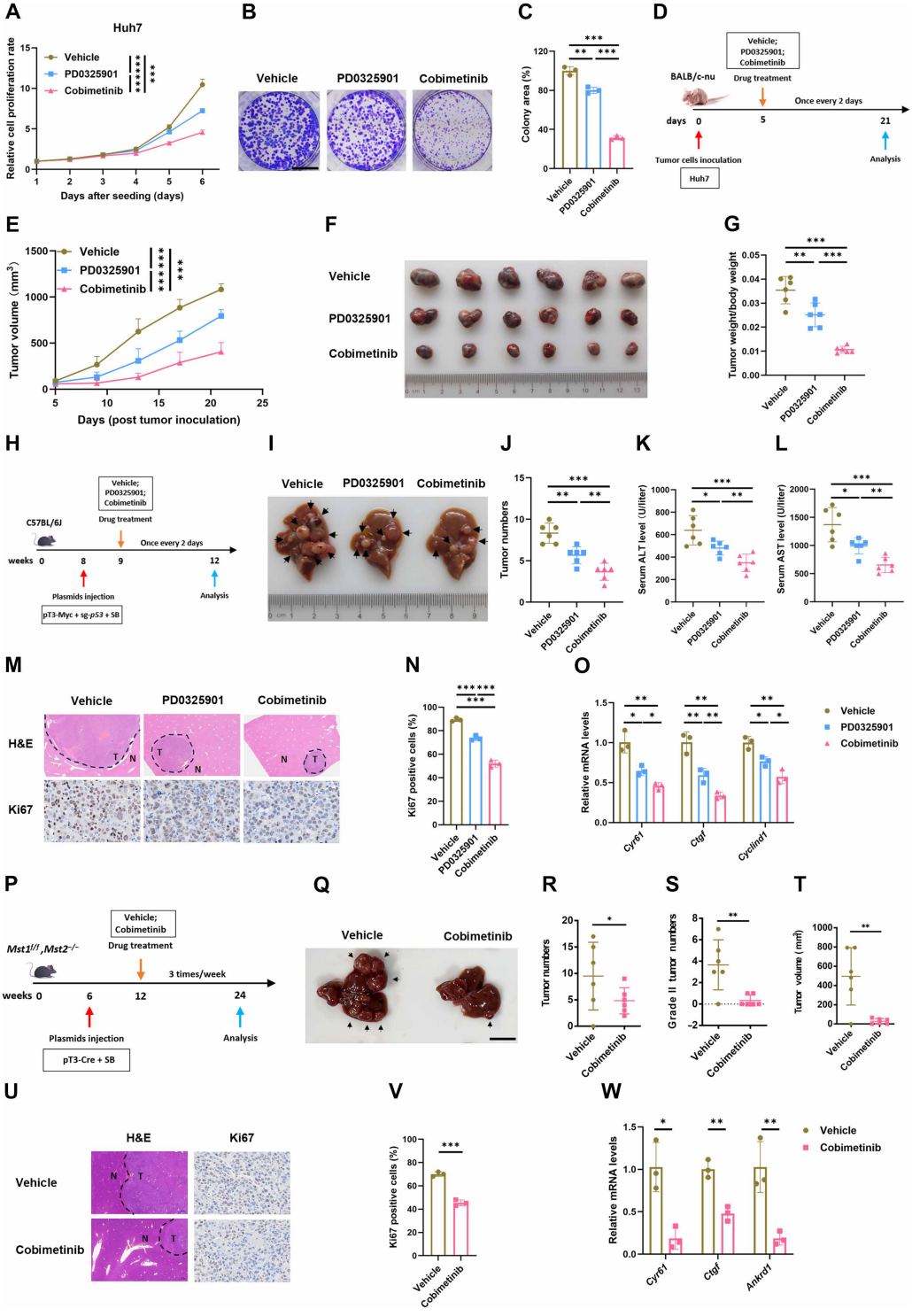

Fig. 5. Cobimetinib suppresses liver tumor growth and tumorigenesis and alleviates liver damage. (**A**) Cell proliferation assay analyzed the effects of vehicle, PD0325901 (0.1 μM), and cobimetinib (0.1 μM) on cell proliferation in Huh7 cells ($n = 6$). (**B**) Colony formation assay assessed the effects of vehicle, PD0325901 (1 μM), and cobimetinib (1 μM) on colony formation in Huh7 cells. Scale bar, 1 cm. (**C**) Quantified relative colony area described in (B) ($n = 3$). (**D**) Treatment diagram for vehicle, PD0325901, and cobimetinib in the Huh7 CDX mice model. (**E**) Tumor growth curve of vehicle, PD0325901 (10 mg/kg), and cobimetinib (10 mg/kg) treatment in the Huh7 CDX mice model ($n = 6$). (**F**) Representative tumor images described in (D) and (E) were documented on day 21 postinoculation. (**G**) The ratio of tumor weight to body weight described in (D) to (F) was calculated on day 21 postinoculation ($n = 6$). (**H**) Treatment diagram for vehicle, PD0325901, and cobimetinib in the *Myc*; sg-*p53*–induced liver tumorigenesis model. (**I**) Representative tumor images of vehicle, PD0325901 (10 mg/kg), and cobimetinib (10 mg/kg) treatment in the *Myc*; sg-*p53*–induced liver tumorigenesis model ($n = 6$). (**J**) Quantified tumor numbers in mice treated with vehicle, PD0325901, and cobimetinib as described in (H) and (I) ($n = 6$). (**K** and **L**) Mice serum ALT (K) and AST (L) concentrations under the impact of vehicle, PD0325901, and cobimetinib as described in (H) and (I) ($n = 6$). (**M**) Representative images of H&E staining and Ki67 IHC described in (H) and (I). Scale bars, 500 μm (H&E) and 20 μm (Ki67). (**N**) Quantified Ki67 signals of the tumor sections analyzed by IHC in (M) ($n = 3$). (**O**) RT-qPCR analyzed the expression of YAP-TEAD target genes *Cyr61*, *Ctgf*, and *Cyclind1* described in (H) and (I) ($n = 3$). (**P**) Treatment diagram for vehicle and cobimetinib in an *Mst1/2* DKO–induced liver tumorigenesis model. (**Q**) Representative tumor images of vehicle and cobimetinib (10 mg/kg) treatment in the *Mst1/2* DKO–induced liver tumor genesis model ($n = 6$). Scale bar, 1 cm. (**R** to **T**) Quantified tumor numbers [(R); $n = 6$], quantified grade II tumor numbers [(S); $n = 6$], and quantified tumor volumes [(T); $n = 6$] in mice treated with vehicle and cobimetinib described in (P) and (Q). (**U**) Representative images of H&E staining and Ki67 IHC described in (P) and (Q). Scale bars, 500 μm (H&E) and 20 μm (Ki67). (**V**) Quantified Ki67 signals in the tumor sections analyzed by IHC in (U) ($n = 3$). (**W**) RT-qPCR analyzed expression of *Cyr61*, *Ctgf*, and *Cyclind1* described in (P) and (Q) ($n = 3$). Data are means ± SD. $^*P < 0.05$; $^{**}P < 0.01$; $^{***}P < 0.001$, Student's *t* test [(R) to (T), (V), and (W)]; one-way ANOVA with Tukey's correction [(A), (C), (E), (G), (J) to (L), (N), and (O)]. See also figs. S15 to S17.

fig. S16B), suggesting that YAP inhibition was crucial for cobimetinib-mediated suppression of liver tumorigenesis.

In addition, an in vivo liver tumorigenesis model induced by YAP hyperactivation was used. As the most important upstream kinase that restricts YAP activation, the inactivation of MST1/2 is responsible for the overactivation of YAP and tumorigenesis (*24*, *25*). By combining a genetically engineered mouse model, $Mst1^{Flox/Flox}$, $Mst2^{-/-}$, with the Sleeping Beauty (SB) system, we established an in vivo liver tumorigenesis

model caused by YAP hyperactivation (Fig. 5P) (*30*). Consistent with the findings in the above Myc; sg-*p53* mice model, cobimetinib treatment reduced liver tumorigenesis in these *Mst1/2* DKO mice compared with the vehicle (Fig. 5Q). It apparently decreased the tumor numbers (Fig. 5R), the number of grade II tumors (Fig. 5S), and the tumor volumes (Fig. 5T). Cobimetinib treatment also resulted in much smaller lesions, decreased cell proliferation, and increased apoptosis compared with the vehicle control, as evidenced by H&E staining, Ki67, and cleaved caspase-3 analysis, respectively (Fig. 5, U and V, and fig. S16C). RT-qPCR or IHC analysis of liver samples indicated that the expression amounts of YAP target genes, such as *Cyr61* and *Ctgf*, were down-regulated by cobimetinib (Fig. 5W and fig. S16C).

Furthermore, a liver tumorigenesis model induced by the coexpression of Nras G12V (Gly^{12}→Val) and Myr-Akt [Nras (G12V); Myr-Akt] was used to evaluate the inhibitory effects of cobimetinib (fig. S17, A to E). In this model, YAP was also activated (*31*). IHC analysis for hepatocyte nuclear factor 4 alpha (HNF4α) and cytokeratin 19 (CK19) was performed to confirm the successful generation of liver tumor (fig. S17D). Compared with both selumetinib and PD0325901, cobimetinib demonstrated superior efficacy with comparable mechanistic activity in suppressing Nras (G12V); Myr-Akt–induced liver tumorigenesis (fig. S17), consistent with the aforementioned models. Collectively, these data indicated that cobimetinib is an effective inhibitor of liver tumorigenesis.

Cobimetinib improves sorafenib and lenvatinib efficacy against liver tumor growth and tumorigenesis

Sorafenib, a broad-spectrum tyrosine kinase inhibitor (TKI) that exerts robust antiangiogenic effects by targeting VEGFR1-3 and PDGFR, has been the standard first-line systemic therapy for advanced HCC for more than a decade. However, the clinical response rate to sorafenib is below 20%, and the overall survival (OS) benefits are limited because of primary or secondary resistance (*32*). The activation of YAP was observed after sorafenib treatment, as assessed by decreased phosphorylation of YAP [pYAP(S127)] and increased expression of the Hippo targets *CYR61* and *CTGF* (fig. S18, A and B). Because the activation of YAP has been reported to contribute to sorafenib resistance in HCC (*33*, *34*), a sorafenib-resistant Huh7 cell line (Huh7-SorR) was subsequently generated and verified through cell viability and colony formation assays to evaluate cobimetinib's efficacy against sorafenib-resistant liver cancer (fig. S18, C to E). Compared with Huh7-WT cells, Huh7-SorR cells exhibited elevated YAP protein abundance. In addition, YAP knockdown increased the sensitivity of Huh7-SorR cells to sorafenib, indicating that YAP plays a critical role in mediating Huh7-SorR tumor growth (fig. S18, F to I). Hence, we conducted the subsequent studies to examine the therapeutic efficacy of combining cobimetinib with sorafenib.

Cobimetinib not only enhanced the effectiveness of sorafenib in inhibiting the cell proliferation or colony formation of human liver cancer cell Huh7 and Huh7-SorR in vitro (Fig. 6, A to C, and fig. S18, J and K) but also suppressed the growth of Huh7 and Huh7-SorR xenograft tumors in vivo with the mechanism of decreasing the proliferation and increasing the apoptosis (Fig. 6, D to G, and fig. S19), all without affecting the body weight of the mice (Fig. 6H). Moreover, cobimetinib monotherapy has demonstrated superior benefits over sorafenib both in vitro and in vivo (Fig. 6, A to G, and fig. S19, A to F), as well as over the TEAD inhibitor TED347 in vivo (Fig. 6, D to G, and fig. S19A). This superiority could stem from cobimetinib's effective targeting of the YAP-TEAD complex.

Furthermore, the combination of cobimetinib and sorafenib demonstrated marked synergistic benefits in the HCC mouse model induced by Myc; sg-*p53* and Nras (G12V); Myr-Akt, inhibiting liver tumorigenesis through mechanisms involving decreased proliferation and increased apoptosis and alleviating liver damage (Fig. 6, I to P, and fig. S20, A to F).

Lenvatinib, a small-molecule inhibitor of multiple receptor tyrosine kinases, is used to treat patients with advanced HCC. However, its overall response rate is only 24.1%, highlighting the need for combination therapies to improve the clinical benefits of lenvatinib-based HCC treatments (*35*). We therefore also evaluated the efficacy of combining cobimetinib with lenvatinib on tumor growth and tumorigenesis in vivo. Although lenvatinib, unlike sorafenib, did not alter pYAP (S127) expression or mRNA abundance of *CYR61* and *CTGF* in Huh7 cells apparently (figs. S18, A and B, and S21, A and B), cobimetinib still exhibited marked cooperative effects with lenvatinib in suppressing Huh7 tumor growth and tumorigenesis through mechanisms akin to those in the sorafenib combination treatment (figs. S20, B to F, and S1, C to H). Cobimetinib inhibited liver tumor growth to a degree comparable to that of lenvatinib alone (fig. S21, C to H). However, it demonstrated superior suppression of liver tumorigenesis compared with lenvatinib (fig. S20, B to F). Collectively, cobimetinib's ability to disrupt the YAP-TEAD interaction improved the efficacy of sorafenib and lenvatinib in suppressing both liver tumor growth and tumorigenesis.

Cobimetinib overcomes MAPK activation–mediated resistance

Hippo pathway–targeted therapies are considered to have great potential for combination with RAS–MAPK pathway inhibitors, owing to the close functional ties in development and disease (*36*). MAPK hyperactivation confers resistance to YAP-TEAD inhibition, and MAPK inhibition improves their efficacy (*37*, *38*). Consistently, we also observed that cobimetinib suppressed cell viability more effectively than VT-104 in NF1 knockdown (fig. S22, A and B) and GNE 7883 (a YAP-TEAD inhibitor)–resistant cell models (fig. S22, C to E), where NF1 loss and TEAD inhibitor resistance correlate with MAPK activation. Therefore, cobimetinib's dual-targeting capability offers distinct advantages over single-pathway inhibitors and investigational YAP-TEAD inhibitors.

DISCUSSION

Over the past 2 decades, substantial progress has been made in drug discovery targeting the Hippo pathway to combat diseases, particularly in tumors. YAP-TEAD protein interactions have emerged as the most promising target for small-molecule modulation (*5*). Various methods and strategies, including fluorescence resonance energy transfer, thermal shift assay, alpha assay, surface plasmon resonance, and in silico molecular docking, have been used to screen for YAP-TEAD inhibitors (*39*). However, the discovered inhibitors remain in the preclinical testing phase. In comparison with existing methods, the CEBIT screening assay presented here offers several noteworthy advantages. First, it detects in vitro biomolecular interactions with highly sensitivity and minimal protein input, inspired by cellular membraneless organelles. Second, it enables high-content imaging analysis of compound effects on the YAP-TEAD interaction, supporting large-scale HTS in 384-well plates. Last, it provides a definitive readout of compound efficacy in directly modulating the purified protein-protein interaction (*7*).

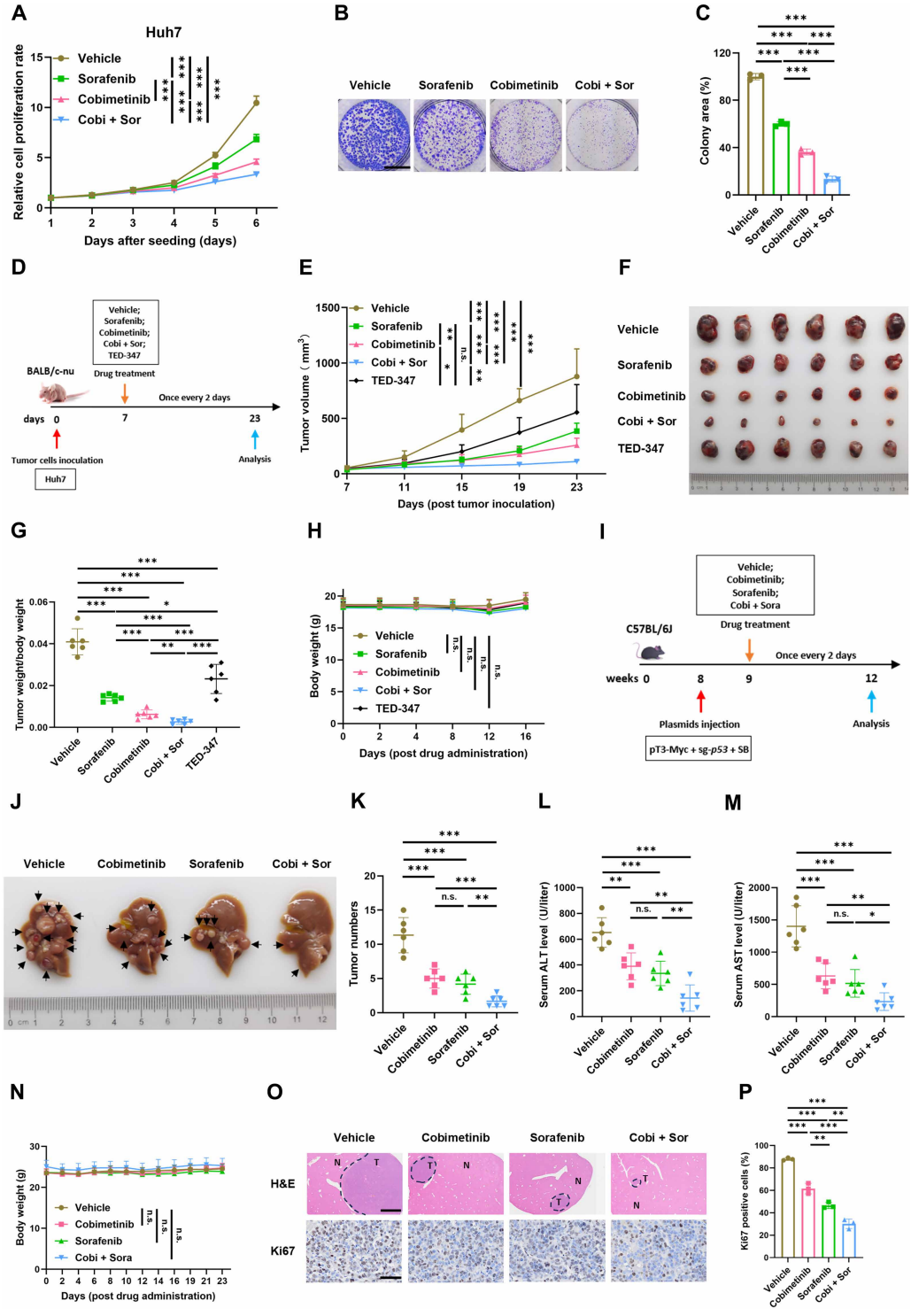

Fig. 6. Cobimetinib improves sorafenib efficacy against both liver tumor growth and tumorigenesis. (**A**) Cell proliferation assay analyzed vehicle, sorafenib (0.1 μM), and cobimetinib (0.1 μM) single or combined treatment on cell proliferation in Huh7 cells ($n = 6$). (**B**) Colony formation assay analysis of vehicle, sorafenib (0.1 μM), and cobimetinib (0.1 μM) single or combined treatment on colony formation in Huh7 cells. Scale bar, 1 cm. (**C**) Quantified relative colony area described in (B) ($n = 3$). (**D**) Treatment diagram for vehicle, TED-347, and single or combined treatment of sorafenib and cobimetinib in the Huh7 CDX tumor growth model. (**E**) Tumor growth curve of vehicle, TED-347 (10 mg/kg), and single or combined treatment of sorafenib (20 mg/kg) and cobimetinib (10 mg/kg) in the Huh7 CDX mice model ($n = 6$). (**F**) Representative tumor images described in (D) and (E) were documented on day 23 postinoculation. (**G**) The ratio of tumor weight to body weight described in (D) to (F) was calculated on day 23 postinoculation ($n = 6$). (**H**) Body weights of mice described in (D) to (G) were measured ($n = 6$). (**I**) Treatment diagram for vehicle and single or combined treatment of sorafenib and cobimetinib in the *Myc*; sg-*p53*–induced liver tumorigenesis model. (**J**) Representative tumor images of vehicle and single or combined treatment of sorafenib (20 mg/kg) and cobimetinib (10 mg/kg) in the *Myc*; sg-*p53*–induced liver tumorigenesis model ($n = 6$). (**K**) Quantified tumor numbers in mice treated with vehicle and single or combined treatment of sorafenib (20 mg/kg) and cobimetinib (10 mg/kg) described in (I) and (J) ($n = 6$). (**L** and **M**) Mice serum ALT (L) and AST (M) concentrations under the impact of vehicle and single or combined treatment of sorafenib (20 mg/kg) and cobimetinib (10 mg/kg) described in (I) and (J) ($n = 6$). (**N**) Body weights of mice described in (I) and (J) were measured ($n = 6$). (**O**) Representative images of H&E and Ki67 staining described in (I) and (J). Scale bars, 500 μm (H&E) and 20 μm (Ki67). (**P**) Quantified Ki67 signals in the tumor sections analyzed by IHC in (O) ($n = 3$). Data are means ± SD. $^*P < 0.05$; $^{**}P < 0.01$; $^{***}P < 0.001$; n.s., not significant; one-way ANOVA with Tukey's correction. See also figs. S18 to S21.

By using the CEBIT method, the clinical drug cobimetinib was identified as a YAP-TEAD inhibitor (fig. S23). Cocrystallization and palmitoylation studies revealed that cobimetinib binds to the central pocket of TEAD, thereby blocking its palmitoylation. This structure offers insights into the inhibition mechanisms of cobimetinib and provides a valuable platform for optimizing inhibitors with enhanced biological and pharmacological activities.

Apart from its direct oncogenic potency in cancers with disrupted Hippo pathways, the YAP/TAZ-TEAD complex substantially contributes to both intrinsic and acquired tumor resistance, which undermines

a wide variety of antitumor treatments. MEK1 mutants occur in more than 1% of human tumors, especially melanoma, colorectal, lung, and other carcinomas (*17*). Here, we analyzed cobimetinib's therapeutic potential against the MEK1 Δ98-103 mutant, a mutation observed in human tumors. Despite resistance to conventional MEK1/2 inhibitors, this mutant demonstrated robust sensitivity to cobimetinib in vitro and in vivo. In addition, A549-TramR and Huh7-SorR cells were also sensitive to cobimetinib in vitro or in vivo. Our in-depth mechanistic study revealed that YAP activity was markedly up-regulated in these cells. However, cobimetinib's distinct ability to disrupt YAP-TEAD, independently of MEK1/2, overcame this resistance and displayed potential in inhibiting tumor growth.

YAP is universally activated by Hippo pathway dysregulation, which is crucial for tumorigenesis across various cancers. Beyond mediating Hippo pathway–induced oncogenesis, YAP can also function downstream of other signaling pathways, becoming abnormally active when they are deregulated. For instance, YAP is activated in uveal melanoma with GNAQ/GNA11 mutations in GPCR signaling (*40*). In APC-deficient colorectal cancer, Wnt-ON elevates YAP abundance, where YAP and β-catenin synergistically promote tumorigenesis (*41*). In this study, we also showed that cobimetinib markedly reduced tumor growth associated with YAP-TEAD hyperactivation, suggesting a potential application of cobimetinib in the therapy of such YAP-TEAD hyperactivation tumors.

HCC is the third leading cause of cancer-related death worldwide. Sorafenib, a broad-spectrum TKI, has been the first-line systemic treatment for advanced HCC for more than a decade. However, its clinical response rate is below 20%, whereas its OS benefits are severely hindered by primary and secondary resistance (*32*). Lenvatinib, another first-line option, also has a low overall response rate, necessitating combination therapies (*35*). In this study, we demonstrated that cobimetinib, alone or combined with sorafenib or lenvatinib, strongly diminished tumor growth, inhibited HCC tumorigenesis, and mitigated liver damage. However, the determination of the optimal dosage for administering this combination treatment remains unexplored, which is a limitation of the study. Nevertheless, our data indicate that cobimetinib, administered alone or in combination with sorafenib or lenvatinib, could be an encouraging therapeutic strategy for HCC management.

This study sheds light on cobimetinib's single and synergistic effects with sorafenib and lenvatinib in suppressing tumor growth and tumorigenesis. However, several limitations should be acknowledged. First, the experimental findings were derived primarily from in vitro and xenograft models, which may not fully reflect human tumor complexity or clinical diversity. Second, clinical translation of these findings requires further validation in patient-derived models or early trials to assess therapeutic efficacy and safety in humans. Last, unaddressed interindividual differences in drug pharmacokinetics and pharmacodynamics could affect clinical outcomes.

In summary, this study introduces a CEBIT-based HTS method for discovering YAP-TEAD inhibitors. The identified clinical drug, cobimetinib, disrupts the YAP-TEAD complex by inhibiting TEAD palmitoylation. Cobimetinib, when administered alone, demonstrates superior efficacy in suppressing the growth of complex cancers with constant YAP activation, YAP hyperactivation, MEK1 Δ98-103 mutation, or drug resistance stemming from YAP activation. In addition, it exhibits a suppressive effect on liver tumorigenesis. Furthermore, it enhances the efficacy of the clinical first-line drug sorafenib and lenvatinib against HCC tumor growth and tumorigenesis. These findings elucidate the mechanisms of cobimetinib's action in complex cancers and expanded its therapeutic horizon in the realm of cancer treatment. The monotherapy of cobimetinib or its combination with sorafenib or lenvatinib holds immense potential as a potent therapeutic strategy in combating complex and resistant cancer types associated with hyperactivated YAP, offering a promising approach to tackling these challenging cancer malignancies.

MATERIALS AND METHODS

Study design

The objectives of this work were to identify and characterize YAP-TEAD inhibitors and evaluate their efficacy on hyperactivated YAP-induced tumor growth and tumorigenesis in multiple cancer models. We developed a phase separation–based HTS method, screening 6365 compounds to find cobimetinib, an FDA-approved MEK1/2 inhibitor, as a potent YAP-TEAD inhibitor. MD, cocrystallization, and palmitoylation studies showed cobimetinib binds to the TEAD LP, disrupting palmitoylation. We also assessed cobimetinib's efficacy in three MAPK-dysregulated, YAP-hyperactivated models, showing superior activity over selumetinib and PD0325901. Moreover, cobimetinib showed promise in inhibiting tumor growth and tumorigenesis in HCC with hyperactivated YAP, alone or with first-line drugs, in mouse models. Although the experiment was not blinded, animals were randomly grouped, with sample sizes set by prior and preliminary data. All cell-based experiments were independently replicated at least three times, and animals were in groups of four to six. Data points were shown as dots in figures to illustrate biological variability, with replicate numbers in legends.

Statistical analyses

Data were analyzed using GraphPad Prism 10 or Excel 2019 software, presented as means ± SD with error bars. Group comparisons used one-way analysis of variance (ANOVA) or unpaired two-tailed Student's *t* test, with significance at $*P < 0.05$; $**P < 0.01$; $***P < 0.001$; n.s., not significant. Statistical details (tests used, *n* values, and precision) were specified in figures and legends unless otherwise indicated.

Supplementary Materials

The PDF file includes:
Materials and Methods
Figs. S1 to S23
Tables S1 to S5
References (*42*–*44*)

Other Supplementary Material for this manuscript includes the following:
Data file S1
MDAR Reproducibility Checklist

REFERENCES AND NOTES

1. Y. Zheng, D. Pan, The Hippo signaling pathway in development and disease. *Dev. Cell* **50**, 264–282 (2019).
2. F. Zanconato, M. Cordenonsi, S. Piccolo, YAP/TAZ at the roots of cancer. *Cancer Cell* **29**, 783–803 (2016).
3. D. D. Shao, W. Xue, E. B. Krall, A. Bhutkar, F. Piccioni, X. Wang, A. C. Schinzel, S. Sood, J. Rosenbluh, J. W. Kim, Y. Zwang, T. M. Roberts, D. E. Root, T. Jacks, W. C. Hahn, KRAS and YAP1 converge to regulate EMT and tumor survival. *Cell* **158**, 171–184 (2014).
4. I. Bado, X. H. F. Zhang, Senesce to survive: YAP-mediated dormancy escapes EGFR/MEK inhibition. *Cancer Cell* **37**, 1–2 (2020).

5. A. V. Pobbati, R. Kumar, B. P. Rubin, W. Hong, Therapeutic targeting of TEAD transcription factors in cancer. *Trends Biochem. Sci.* **48**, 450–462 (2023).
6. D. Cai, D. Feliciano, P. Dong, E. Flores, M. Gruebele, N. Porat-Shliom, S. Sukenik, Z. Liu, J. Lippincott-Schwartz, Phase separation of YAP reorganizes genome topology for long-term YAP target gene expression. *Nat. Cell Biol.* **21**, 1578–1589 (2019).
7. M. Zhou, W. Li, J. Li, L. Xie, R. Wu, L. Wang, S. Fu, W. Su, J. Hu, J. Wang, P. Li, Phase-separated condensate-aided enrichment of biomolecular interactions for high-throughput drug screening in test tubes. *J. Biol. Chem.* **295**, 11420–11434 (2020).
8. W. Tian, J. Yu, D. R. Tomchick, D. Pan, X. Luo, Structural and functional analysis of the YAP-binding domain of human TEAD2. *Proc. Natl. Acad. Sci. U.S.A.* **107**, 7293–7298 (2010).
9. S. Jiao, H. Wang, Z. Shi, A. Dong, W. Zhang, X. Song, F. He, Y. Wang, Z. Zhang, W. Wang, X. Wang, T. Guo, P. Li, Y. Zhao, H. Ji, L. Zhang, Z. Zhou, A peptide mimicking VGLL4 function acts as a YAP antagonist therapy against gastric cancer. *Cancer Cell* **25**, 166–180 (2014).
10. T. T. Tang, A. W. Konradi, Y. Feng, X. Peng, M. Ma, J. Li, F. X. Yu, K. L. Guan, L. Post, Small molecule inhibitors of TEAD auto-palmitoylation selectively inhibit proliferation and tumor growth of *NF2*-deficient mesothelioma. *Mol. Cancer Ther.* **20**, 986–998 (2021).
11. J.-H. Zhang, T. D. Y. Chung, K. R. Oldenburg, A simple statistical parameter for use in evaluation and validation of high throughput screening assays. *SLAS Discov.* **4**, 67–73 (1999).
12. W. Xu, G. Pei, H. Liu, X. Ju, J. Wang, Q. Ding, P. Li, Compartmentalization-aided interaction screening reveals extensive high-order complexes within the SARS-CoV-2 proteome. *Cell Rep.* **36**, 109482 (2021).
13. B. Zhao, X. Wei, W. Li, R. S. Udan, Q. Yang, J. Kim, J. Xie, T. Ikenoue, J. Yu, L. Li, P. Zheng, K. Ye, A. Chinnaiyan, G. Halder, Z. C. Lai, K. L. Guan, Inactivation of YAP oncoprotein by the Hippo pathway is involved in cell contact inhibition and tissue growth control. *Genes Dev.* **21**, 2747–2761 (2007).
14. P. Chan, X. Han, B. Zheng, M. DeRan, J. Yu, G. K. Jarugumilli, H. Deng, D. Pan, X. Luo, X. Wu, Autopalmitoylation of TEAD proteins regulates transcriptional output of the Hippo pathway. *Nat. Chem. Biol.* **12**, 282–289 (2016).
15. K. P. Garnock-Jones, Cobimetinib: First global approval. *Drugs* **75**, 1823–1830 (2015).
16. H. Xu, S. Zhou, H. Xia, H. Yu, Q. Tang, F. Bi, MEK nuclear localization promotes YAP stability via sequestering β-TrCP in KRAS mutant cancer cells. *Cell Death Differ.* **26**, 2400–2415 (2019).
17. Y. Gao, M. T. Chang, D. McKay, N. Na, B. Zhou, R. Yaeger, N. M. Torres, K. Muniz, M. Drosten, M. Barbacid, G. Caponigro, D. Stuart, H. Moebitz, D. B. Solit, O. Abdel-Wahab, B. S. Taylor, Z. Yao, N. Rosen, Allele-specific mechanisms of activation of MEK1 mutants determine their properties. *Cancer Discov.* **8**, 648–661 (2018).
18. A. Aharonov, A. Shakked, K. B. Umansky, A. Savidor, A. Genzelinakh, D. Kain, D. Lendengolts, O. Y. Revach, Y. Morikawa, J. Dong, Y. Levin, B. Geiger, J. F. Martin, E. Tzahor, ERBB2 drives YAP activation and EMT-like processes during cardiac regeneration. *Nat. Cell Biol.* **22**, 1346–1356 (2020).
19. G. E. Coggins, A. Farrel, K. S. Rathi, C. M. Hayes, L. Scolaro, J. L. Rokita, J. M. Maris, YAP1 mediates resistance to MEK1/2 inhibition in neuroblastomas with hyperactivated RAS signaling. *Cancer Res.* **79**, 6204–6214 (2019).
20. W. Y. Zhang, N. Nandakumar, Y. H. Shi, M. Manzano, A. Smith, G. Graham, S. Gupta, E. E. Vietsch, S. Z. Laughlin, M. Wadhwa, M. Chetram, M. Joshi, F. Wang, B. Kallakury, J. Toretsky, A. Wellstein, C. L. Yi, Downstream of mutant KRAS, the transcription regulator YAP is essential for neoplastic progression to pancreatic ductal adenocarcinoma. *Sci. Signal.* **7**, ra42 (2014).
21. Y. Wang, Y. Zhu, Y. Gu, M. Ma, Y. Wang, S. Qi, Y. Zeng, R. Zhu, X. Wang, P. Yu, J. Xu, Y. Shu, F.-X. Yu, Stabilization of Motin family proteins in NF2-deficient cells prevents full activation of YAP/TAZ and rapid tumorigenesis. *Cell Rep.* **36**, 109596 (2021).
22. Z. Qiu, H. Li, Z. Zhang, Z. Zhu, S. He, X. Wang, P. Wang, J. Qin, L. Zhuang, W. Wang, F. Xie, Y. Gu, K. Zou, C. Li, C. Li, C. Wang, J. Cen, X. Chen, Y. Shu, Z. Zhang, L. Sun, L. Min, Y. Fu, X. Huang, H. Lv, H. Zhou, Y. Ji, Z. Zhang, Z. Meng, X. Shi, H. Zhang, Y. Li, L. Hui, A pharmacogenomic landscape in human liver cancers. *Cancer Cell* **36**, 179–193.e11 (2019).
23. J. Dong, G. Feldmann, J. Huang, S. Wu, N. Zhang, S. A. Comerford, M. F. Gayyed, R. A. Anders, A. Maitra, D. Pan, Elucidation of a universal size-control mechanism in *Drosophila* and mammals. *Cell* **130**, 1120–1133 (2007).
24. D. W. Zhou, C. Conrad, F. Xia, J. S. Park, B. Payer, Y. Yin, G. Y. Lauwers, W. Thasler, J. T. Lee, J. Avruch, N. Bardeesy, Mst1 and Mst2 maintain hepatocyte quiescence and suppress hepatocellular carcinoma development through inactivation of the Yap1 oncogene. *Cancer Cell* **16**, 425–438 (2009).
25. H. Song, K. K. Mak, L. Topol, K. S. Yun, J. X. Hu, L. Garrett, Y. B. Chen, O. Park, J. Chang, R. M. Simpson, C. Y. Wang, B. Gao, J. Jiang, Y. Z. Yang, Mammalian Mst1 and Mst2 kinases play essential roles in organ size control and tumor suppression. *Proc. Natl. Acad. Sci. U.S.A.* **107**, 1431–1436 (2010).
26. U. J. Yun, S. J. Bae, Y. R. Song, Y. W. Kim, A critical YAP in malignancy of HCC is regulated by evodiamine. *Int. J. Mol. Sci.* **23**, 1855 (2022).
27. L. Xu, P. Li, X. Hao, Y. Lu, M. Liu, W. Song, L. Shan, J. Yu, H. Ding, S. Chen, A. Yang, Y. A. Zeng, L. Zhang, H. Jiang, SHANK2 is a frequently amplified oncogene with evolutionarily conserved roles in regulating Hippo signaling. *Protein Cell* **12**, 174–193 (2021).
28. D. F. Tschaharganeh, X. Chen, P. Latzko, M. Malz, M. M. Gaida, K. Felix, S. Ladu, S. Singer, F. Pinna, N. Gretz, C. Sticht, M. L. Tomasi, S. Delogu, M. Evert, B. Fan, S. Ribback, L. Jiang, S. Brozzetti, F. Bergmann, F. Dombrowski, P. Schirmacher, D. F. Calvisi, K. Breuhahn, Yes-associated protein up-regulates Jagged-1 and activates the Notch pathway in human hepatocellular carcinoma. *Gastroenterology* **144**, 1530–1542.e12 (2013).
29. Y. Sun, H. Wei, W. Yu, H. Gao, J. Li, X. Li, H. Zhang, H. Zhang, S. Miao, L. Zhao, R. Yang, J. Xu, Y. Lu, F. Wei, H. Zhou, D. Gao, Y. Jin, L. Zhang, The actin-binding protein drebrin disrupts NF2-LATS kinases complex assembly to facilitate liver tumorigenesis. *Hepatology* **81**, 1433–1451 (2025).
30. X. Feng, T. Lu, J. Li, R. Yang, L. Hu, Y. Ye, F. Mao, L. He, J. Xu, Z. Wang, Y. Liu, Y. Zhang, H. Ji, Y. Zhao, S. Cheng, W. Tian, L. Zhang, The tumor suppressor interferon regulatory factor 2 binding protein 2 regulates Hippo pathway in liver cancer by a feedback loop in mice. *Hepatology* **71**, 1988–2004 (2020).
31. H. Wang, J. Wang, S. Zhang, J. Jia, X. Liu, J. Zhang, P. Wang, X. Song, L. Che, K. Liu, S. Ribback, A. Cigliano, M. Evert, H. Wu, D. F. Calvisi, Y. Zeng, X. Chen, Distinct and overlapping roles of Hippo effectors YAP and TAZ during human and mouse hepatocarcinogenesis. *Cell. Mol. Gastroenterol. Hepatol.* **11**, 1095–1117 (2021).
32. J. M. Llovet, S. Ricci, V. Mazzaferro, P. Hilgard, E. Gane, J.-F. Blanc, A. C. de Oliveira, A. Santoro, J.-L. Raoul, A. Forner, M. Schwartz, C. Porta, S. Zeuzem, L. Bolondi, T. F. Greten, P. R. Galle, J.-F. Seitz, I. Borbath, D. Häussinger, T. Giannaris, M. Shan, M. Moscovici, D. Voliotis, J. Bruix, SHARP Investigators Study Group, Sorafenib in advanced hepatocellular carcinoma. *N. Engl. J. Med.* **359**, 378–390 (2008).
33. T. Sun, W. Mao, H. Peng, Q. Wang, L. Jiao, YAP promotes sorafenib resistance in hepatocellular carcinoma by upregulating survivin. *Cell. Oncol.* **44**, 689–699 (2021).
34. J. Wu, H. Chai, F. Li, Q. Ren, Y. Gu, SETD1A augments sorafenib primary resistance via activating YAP in hepatocellular carcinoma. *Life Sci.* **260**, 118406 (2020).
35. M. Kudo, R. S. Finn, S. Qin, K. H. Han, K. Ikeda, F. Piscaglia, A. Baron, J. W. Park, G. Han, J. Jassem, J. F. Blanc, A. Vogel, D. Komov, T. R. J. Evans, C. Lopez, C. Dutcus, M. Guo, K. Saito, S. Kraljevic, T. Tamai, M. Ren, A. L. Cheng, Lenvatinib versus sorafenib in first-line treatment of patients with unresectable hepatocellular carcinoma: A randomised phase 3 non-inferiority trial. *Lancet* **391**, 1163–1173 (2018).
36. K. F. Harvey, T. T. Tang, Targeting the Hippo pathway in cancer. *Nat. Rev. Drug Discov.* **24**, 852–869 (2025).
37. S. Paul, T. J. Hagenbeek, J. Tremblay, V. Kameswaran, C. Ong, C. Liu, A. D. Guarnaccia, J. A. Mondo, P. L. Hsu, N. M. KJavin, B. Czech, J. Smola, D. A. H. Nguyen, J. A. Lacap, T. H. Pham, Y. Liang, R. A. Blake, L. Gerosa, M. Grimmer, S. Xie, B. Daniel, X. Yao, A. Dey, Cooperation between the Hippo and MAPK pathway activation drives acquired resistance to TEAD inhibition. *Nat. Commun.* **16**, 1743 (2025).
38. A. Kulkarni, V. Mohan, T. T. Tang, L. Post, Y.-C. Chan, M. Manning, N. Thio, B. L. Parker, M. A. Dawson, J. Rosenbluh, J. H. A. Vissers, K. F. Harvey, Identification of resistance mechanisms to small-molecule inhibition of TEAD-regulated transcription. *EMBO Rep.* **25**, 3944–3969 (2024).
39. K. Nouri, T. Azad, M. Ling, H. J. J. van Rensburg, A. Pipchuk, H. Shen, Y. Hao, J. Zhang, X. Yang, Identification of celastrol as a novel YAP-TEAD inhibitor for cancer therapy by high throughput screening with ultrasensitive *YAP/TAZ–TEAD* biosensors. *Cancers* **11**, 1596 (2019).
40. F. X. Yu, J. Luo, J. S. Mo, G. Liu, Y. C. Kim, Z. Meng, L. Zhao, G. Peyman, H. Ouyang, W. Jiang, J. Zhao, X. Chen, L. Zhang, C. Y. Wang, B. C. Bastian, K. Zhang, K. L. Guan, Mutant Gq/11 promote uveal melanoma tumorigenesis by activating YAP. *Cancer Cell* **25**, 822–830 (2014).
41. L. Azzolin, T. Panciera, S. Soligo, E. Enzo, S. Bicciato, S. Dupont, S. Bresolin, C. Frasson, G. Basso, V. Guzzardo, A. Fassina, M. Cordenonsi, S. Piccolo, YAP/TAZ incorporation in the β-catenin destruction complex orchestrates the Wnt response. *Cell* **158**, 157–170 (2014).
42. Z. Cao, Y. Hou, Z. Zhao, H. Zhang, L. Tian, Y. Zhang, C. Dong, F. Guo, L. Tan, Y. Han, W. Wang, S. Jiao, Y. Tang, L. An, Z. Zhou, Reactivating Hippo by drug compounds to suppress gastric cancer and enhance chemotherapy sensitivity. *J. Biol. Chem.* **300**, 107311 (2024).
43. S. Liu, Q. Zou, J. P. Chen, X. Yao, P. Guan, W. Liang, P. Deng, X. Lai, J. Yin, J. Chen, R. Chen, Z. Yu, R. Xiao, Y. Sun, J. H. Hong, H. Liu, H. Lu, J. Chen, J. X. Bei, J. Koh, J. Y. Chan, B. Wang, T. Kang, Q. Yu, B. T. Teh, J. Liu, Y. Xiong, J. Tan, Targeting enhancer reprogramming to mitigate MEK inhibitor resistance in preclinical models of advanced ovarian cancer. *J. Clin. Invest.* **131**, e145035 (2021).
44. S. Qi, Y. Zhu, X. Liu, P. Li, Y. Wang, Y. Zeng, A. Yu, Y. Wang, Z. Sha, Z. Zhong, R. Zhu, H. Yuan, D. Ye, S. Huang, C. Ling, Y. Xu, D. Zhou, L. Zhang, F.-X. Yu, WWC proteins mediate LATS1/2 activation by Hippo kinases and imply a tumor suppression strategy. *Mol. Cell* **82**, 1850–1864.e7 (2022).

Acknowledgments: We greatly appreciate F. Yu (Fudan University, Shanghai) for providing NCI-H2052, NCI-H2373, and NCI-H2452 cell lines, as well as Nras (G12V) and Myr-Akt plasmids; W. Tao (Fudan University, Shanghai) for *Mst1*$^{f/f}$, *Mst2*$^{-/-}$ mice; and Z. Qiu (Fudan University, Shanghai) for LIMORE database details. We also thank the Chemical Biology Core Facility at SIBCB for technical assistance in drug screening and the Core Facility and Service Center for School of Life Sciences and Biotechnology, SJTU. **Funding:** Our work was funded by grants

from the National Natural Science Foundation of China (nos. 32221002, 32293233, and 32030025 to L.Z., 32470772 to J.Y., 32370751 to Y.J., 31970672 and 32270877 to X.H., and 82225041 to X.Q.), the National Key R&D Program of China (2020YFA0803201 to X.H.), and the Shanghai Municipal Science and Technology Major Project; Shanghai Leading Talents Program to L.Z. **Author contributions:** R.Y. conducted HTS and analyzed cobimetinib's effects in vitro and in vivo. Jing Wang designed the CEBIT-based HTS and CoPIC-based PPI system in cellulo under P.L.'s guidance. L. Hu and M.W. performed protein purification, MST, structure determination, and in vitro palmitoylation experiment under X.H.'s guidance. Jia Wang and L.Y. helped to analyze cobimetinib in the CDX tumor growth model. L. He and W.Y. helped to analyze cobimetinib in the *Mst1/2* DKO–induced liver tumorigenesis model. X.L., J.H., and F.H. conducted MD analysis. H.G. and X.W. helped to analyze cobimetinib in the Myc; sg-*p53*–induced liver tumorigenesis model. P.C. synthesized the biotin-cobimetinib under X.Q.'s advice. Haijiao Zhang, Haoen Zhang, Y.S., and J.X. provided regents and comments. R.Y., J.Y., and L.Z. wrote the manuscript with input from all authors. All authors were involved in manuscript revising and gave the final approval of the manuscript. L.Z. oversaw the study. **Competing interests:** L.Z., X.H., J.Y., R.Y., and L. Hu hold patent no. 202510096197.1 for cobimetinib as a YAP-TEAD inhibitor, titled "Application of a Drug in Inhibiting the Activity of the YAP-TEAD Transcriptional Complex." The other authors declare that they have no competing interests. **Data, code, and materials availability:** All data associated with this study are present in the paper or the Supplementary Materials. The cobimetinib-TEAD2$_{YBD}$ complex structure is in the PDB (PDB: 8YGQ). The MD simulation code and ligand force field parameters are available under a CC BY-NC 4.0 license at https://doi.org/10.5281/zenodo.19283893. All materials used or generated in this study are commercially available or will be supplied upon reasonable request.

Submitted 23 October 2024
Resubmitted 4 December 2025
Accepted 1 April 2026
Published 22 April 2026
10.1126/scitranslmed.adu0814

Post date 15 July 2026

Erratum for the Research Article "Phase separation–based HTS identifies cobimetinib as a YAP-TEAD inhibitor that suppresses hyperactivated YAP-induced cancer progression"

The authors of the Research Article "Phase separation–based HTS identifies cobimetinib as a YAP-TEAD inhibitor that suppresses hyperactivated YAP-induced cancer progression" by R. Yang *et al*. present one correction and two clarifications in the Supplementary Materials. In fig. S5, the values for 0.37 μM GNE-7883 in NCI-H2052 and NCI-H2373 cells were identical to those for 0.04 μM because of a copy-paste error. The authors retrieved the original data and corrected fig. S5 in the Supplementary Materials PDF and the data in data file S1. Some controls or samples were processed in the same experimental batch to minimize batch-to-batch variability and conserve samples. However, the data were presented in different figure panels for addressing distinct biological questions. To avoid misinterpretation, notations indicating concurrent samples have been added to data file S1 as follows: asterisk (*) for Fig. 4, N and O; asterisk (*) and hash tag (#) for Figs. 5A and 6A; and color marks for fig. S3A. In addition, the full-precision decimal values, raw measurements, and the calculation formula for fig. S21D are provided in data file S1 to avoid misinterpretation caused by rounding. The correction and clarifications do not affect the interpretation of the experiments or conclusions of the study.

Science Translational Medicine

Phase separation–based HTS identifies cobimetinib as a YAP-TEAD inhibitor that suppresses hyperactivated YAP-induced cancer progression

Ruizeng Yang, Liqiao Hu, Jing Wang, Jia Wang, Liang Yuan, Mengying Wu, Lingli He, Wentao Yu, Peihao Chen, Xiaoli Lu, Fangzheng Hu, Haijiao Zhang, Haoran Gao, Xiaodong Wang, Haoen Zhang, Yang Sun, Jinjin Xu, Jing Huang, Hu Zhou, Jidong Zhu, Fang Wei, Yunyun Jin, Yijun Gao, Qiang Fu, Xiangbing Qi, Jing Yu, Pilong Li, Xiaojing He, and Lei Zhang

Sci. Transl. Med. **18** (846), eadu0814. DOI: 10.1126/scitranslmed.adu0814

Editor's summary

YAP/TAZ are key effectors of the Hippo pathway, which regulates an array of biological processes, including cell proliferation, survival, apoptosis, and tissue homeostasis. The binding of YAP/TAZ to the transcription factor TEAD induces the transcription of genes that promote cancer growth. Yang *et al.* showed, using a CEBIT-based high-throughput screening method, that the MEK1/2 inhibitor cobimetinib could be repurposed to bind the TEAD lipid pocket and thereby disrupt the activity of the YAP-TEAD complex. Cobimetinib could reduce tumor growth or tumorigenesis in mouse models of hepatocellular carcinoma and lung cancer. This work suggests a potential therapeutic strategy for cancers with hyperactivated YAP/TAZ signaling. —Amy E. Baek